OPTIMIZING PORT GEOMETRY AND EXHAUST LEAD ANGLE IN OPPOSED PISTON ENGINES

by

Beau Burbrink

A Thesis

Submitted to the Faculty of Purdue University

In Partial Fulfillment of the Requirements for the degree of

Master of Science

School of Engineering Technology

West Lafayette, Indiana

December 2021

THE PURDUE UNIVERSITY GRADUATE SCHOOL
STATEMENT OF COMMITTEE APPROVAL

Dr. Jason Ostanek, Chair

Department of Engineering Technology

Dr. Henry Zhang

Department of Engineering Technology

Dr. Peng Hao Wang

Department of Aviation Technology

Approved by:

Dr. Duane Dunlap

Dedicated to my family, who have supported me throughout my academic career.

ACKNOWLEDGMENTS

I wish to acknowledge the help provided by my major professor, Dr. Jason Ostanek, for providing the resources to complete the computational portion of this research and for his instruction and guidance while learning the process of performing a CFD analysis. I also would like to thank my committee for their astute feedback, which improved my research project. Additionally, I would like to thank my lab mate, James Rieser, for his help defining the cylinder geometry, and Luis Carlos Maldonado Jaime, for his assistance setting up the job scripting on the Purdue RCAC compute cluster.

TABLE OF CONTENTS

LIST OF TABLES

LIST OF FIGURES

LIST OF ABBREVIATIONS

CAD	Computer Aided Design
CFD	Computational Fluid Dynamics
EGR	Exhaust Gas Recirculation
EIA	Energy Information Administration
EPA	Environmental Protection Agency
EPC	Exhaust Port Closing
EPO	Exhaust Port Opening
FOA	Funding Opportunity Announcement
HC	Hydrocarbon
IC	Internal Combustion
IDC	Inner Dead Center
IPC	Intake Port Closing
IPO	Intake Port Opening
MPG	Miles per Gallon
OAT	One-at-a-time Sensitivity Analysis
ODC	Outer Dead Center
OP	Opposed Piston
OP2S	Opposed Piston, Two Stroke
RPM	Rotations per Minute
TKE	Turbulent Kinetic Energy
UDF	User-defined Function

NOMENCLATURE

Symbols:

a	Connecting rod length, m
A	Area of circulation contour, m^2
A_{XZ}	Area of XZ circulation contour, m^2
A_{YZ}	Area of YZ circulation contour, m^2
C	Circulation, m^2/s
C_{swirl}	Swirl circulation, m^2/s
$\widetilde{C_{swirl}}$	Normalized swirl circulation
C_{tumble}	Tumble circulation, m^2/s
$\widetilde{C_{tumble}}$	Normalized tumble circulation
D_{AB}	Diffusion coefficient, m^2/s
d_{bore}	Bore diameter, m
L	Delivery ratio
l	Position along circulation contour, m
LHV_{fuel}	Lower heating value of fuel, J/kg
m	Wiebe parameter
M_A	Molar mass of gas A, g/mol
M_B	Molar mass of gas B, g/mol
m_c	Total air mass in cylinder, kg
m_d	Mass of delivered fresh charge, kg
m_{fuel}	Mass of fuel in cylinder, kg
m_{ref}	Reference mass, kg
m_t	Mass of trapped fresh charge, kg
p	Air pressure, Pa
Q_{ht}	Instantaneous heat transfer, J
Q_n	Heat input due to combustion, J
r	Crank radius, m

Greek:

β	Exhaust piston lead angle, °
$\Delta\theta$	Duration of combustion, °
ε_A/κ	Lennard-Jones parameter of gas A, K
ε_{AB}/κ	Combined Lennard-Jones parameter, Å
ε_B/κ	Lennard-Jones parameter of gas B, K
η_{comb}	Combustion efficiency
η_s	Scavenging efficiency
η_t	Trapping efficiency
θ	Crank angle, °
θ_0	Start of combustion crank angle, °
μ_τ	Friction velocity, m/s
ρ	Flow density, kg/m^3
σ_A	Lennard-Jones parameter of gas A, Å
σ_{AB}	Combined Lennard-Jones parameter, Å
σ_B	Lennard-Jones parameter of gas B, Å
τ_{wall}	Wall shear stress, Pa
υ	Kinematic viscosity, m^2/s
ω_{crank}	Crank speed, RPM
$\Omega_{D,AB}$	Collision integral (Diffusion)

S	Maximum sensitivity coefficient
$\hat{S}_i$	Sensitivity coefficient
T	Air temperature, K
T^*	Diffusion normalized temperature
TKE	Turbulent kinetic energy, m^2/s^2
$\widetilde{TKE}$	Normalized turbulent kinetic energy
U	Velocity vector, m/s
V_{mean}	Mean piston velocity, m/s
x	Crank position relative to ODC, m
x_b	Burned mass fraction (Wiebe)
X_i	Input parameter angle, °
y	Distance from wall, m
y^+	Turbulence parameter
Y_i	Output parameter value

ABSTRACT

A growing global population and improved standard of living in developing countries have resulted in an unprecedented increase in energy demand over the past several decades. While renewable energy sources are increasing, a huge portion of energy is still converted into useful work using heat engines. The combustion process in diesel and petrol engines releases carbon dioxide and other greenhouse gases as an unwanted side-effect of the energy conversion process. By improving the efficiency of internal combustion engines, more chemical energy stored in petroleum resources can be realized as useful work and, therefore, reduce global emissions of greenhouse gases. This research focused on improving the thermal efficiency of opposed-piston engines, which, unlike traditional reciprocating engines, do not use a cylinder head. The cylinder head is a major source of heat loss in reciprocating engines. Therefore, the opposed-piston engine has the potential to improve overall engine efficiency relative to inline or V-configuration engines.

The objective of this research project was to further improve the design of opposed-piston engines by using computational fluid dynamics (CFD) modeling to optimize the engine geometry. The CFD method investigated the effect of intake port geometry and exhaust piston lead angle on the scavenging process and in-cylinder turbulence. After the CFD data was analyzed, scavenging efficiency was found insensitive to transfer port geometry and exhaust piston lead angle with a maximum change of 0.61%. Trapping efficiency was altered exclusively by exhaust piston lead angle and changed from 18% to 26% as the lead angle was increased. The in-cylinder turbulence parameters of the engine (normalized swirl circulation, normalized tumble circulation, and normalized TKE) experienced more complex relationships. All turbulence parameters were sensitive to changing transfer port geometry and exhaust piston lead angle. Some examples of trends seen during the analysis include: an increase in normalized swirl circulation from 0.01 to 4.45 due to changes in swirl angle, a change in normalized tumble circulation from -28.52 to 21.11 as swirl angle increased, and an increase in normalized tumble circulation from 14.20 to 33.68 as exhaust piston lead angle was increased. Based on the present work, an optimum configuration was identified for a swirl angle of 15°, a tilt angle of 10°, and an exhaust piston lead angle of 20°. Future work includes expanding the numerical model's domain to support a complete cylinder-port configuration, adding combustion products to the diffusivity equation in the UDF, and running additional test cases to describe the entire input space for the sensitivity analysis.

CHAPTER 1. INTRODUCTION

Chapter One is an overview of the opposed-piston, two-stroke engine architecture, and the research project's investigatory goals. As the research problem was developed, the project's scope, assumptions, limitations, and delimitations were defined as well.

1.1. Problem Statement

Current projections, made by the United Nations (2019), predict that the world population will continue to increase until 2100. At this point, the world population is expected to peak and hold at approximately 14 billion (United Nations, 2019). Figure 1.1 presents the world population from 1950 to 2100. As the population increases, the world's energy demand correlates.

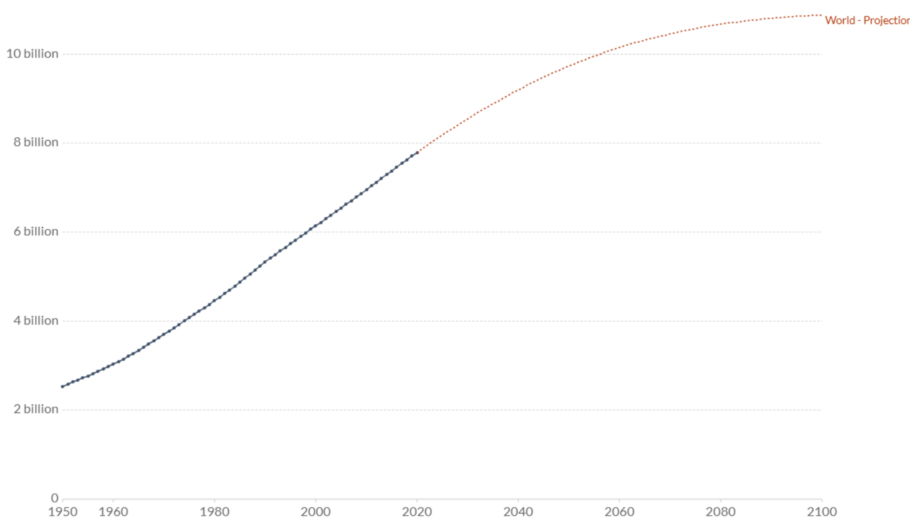

Figure 1.1. Projected world population from 1950 to 2100 (United Nations, 2019).

The world's energy consumption has continued to increase in recent years. According to the U.S. Energy Information Administration (EIA), since 2010, world energy consumption has risen 17% (U.S. Energy Information Administration, 2019). The projected increase of energy consumption is mainly confined to Africa, the Middle East, and Asia, where technology is advancing quickly, and populations are increasing the fastest (U.S. Energy Information Administration, 2019; United Nations, 2019). From today's current energy consumption of

6.5×10^{11} gigajoules, energy consumption is expected to increase an additional 46% (U.S. Energy Information Administration, 2019).

The problem addressed by this project is the production of CO_2 emissions and the fuel consumption rate of modern internal combustion engines. The production of CO_2 emissions by internal combustion engines is one of the top research areas in engine development today (Dalla et al., 2018). The research in CO_2 emissions output is spurred by the increase in CO_2 production over the past 60 years. CO_2 concentrations in the atmosphere have increased by approximately 20% since 1958 (NASA, 2015). The transportation sector is the leading contributor to these emissions. In 2018, the United States recorded the transportation sector producing 28% of the total CO_2 produced by industries (Environmental Protection Agency, 2020).

Fuel economy is another important facet of modern internal combustion engines. Fontaras et al. (2017) state within their research that fuel consumption is the performance metric that gets the most attention from the public, environmental organizations, and consumer organizations. Reducing fuel consumption also reduces CO_2 emissions. When burning hydrocarbon fuels, the bonds between the hydrogen and carbon atoms are broken. This process causes rapid expansion in the engine, which produces power. Once the bonds are broken, the hydrogen and carbon atoms combine with oxygen atoms from the air, creating CO_2 and H_2O.

By reducing the amount of hydrocarbon fuel and air burned, the engine's CO_2 production decreases. Reducing the production of CO_2 by internal combustion engines is significant because CO_2 is a greenhouse gas. By simply doubling the atmospheric CO_2 concentration, compared to pre-industrial levels, the global average temperature would increase by one degree Celsius (National Academy of Sciences, 2014). Also, future legislation will require vehicle manufacturers to meet more stringent regulations for fleet fuel economy. In 2025, U.S. manufacturers will have to attain a fleet-wide average fuel economy of 40.6 miles per gallon (Zielinski et al., 2018).

1.2. Purpose Statement

The purpose of the project was to develop a computational fluid dynamics (CFD) model capable of simulating air flow in an opposed-piston, two-stroke engine. The model was used to analyze flow patterns within the engine and to quantify the effect of different geometric engine parameters on engine performance.

1.2.1. Research Questions

The first research question addressed in the present work was: What was the effect of transfer port geometry and exhaust piston lead angle on scavenging and trapping efficiency?

The second research question addressed in the present work was: What was the effect of transfer port geometry and exhaust piston lead angle on turbulence in the cylinder?

A computational fluid dynamics model with dynamic meshing was used to simulate the time-dependent scavenging process to analyze the engine's response to changes in port geometry and exhaust piston lead angle. A sensitivity analysis was conducted to quantify the effect of geometric parameters and lead angle on scavenging and trapping efficiencies as well as turbulence within the cylinder.

1.2.2. Project Scope

The scope of this project included developing the CFD model, determining model requirements such as fundamental equations and boundary conditions, and evaluating the effects of engine parameters on scavenging and trapping efficiency. A commercial software, ANSYS Fluent, was used for CFD modeling and utilized dynamic meshing and mesh interfaces to investigate the opposed-piston engine's transient operation. The model captured flow characteristics while the pistons were in motion. Once the flow characteristics were captured, the results were analyzed to quantify the significance of each engine parameter on engine efficiency.

1.3. Significance of the Purpose

Researching the operation of an opposed-piston, two-stroke engine was significant because it could allow the use of two-stroke engines in modern vehicles. By improving the trapping and scavenging efficiencies of a two-stroke engine, the power output and engine efficiency are improved (Mattarelli et al., 2017). Also, two-stroke engines are more power-dense since they double the number of power strokes when operating at the same rotational speed. Therefore, developing an emissions-viable, two-stroke engine would increase power-to-weight ratios (Hooper et al., 2011).

Another significant aspect of this project was its current relevance in internal combustion research. For the fiscal year 2020, the United States Department of Energy released a funding opportunity announcement (FOA) for opposed-piston, two-stroke engines (Department of Energy, 2020). This FOA quoted the increased power density and a two-stroke engine's ability to smooth engine transients in an electric hybrid configuration as the main drivers for future research (Department of Energy, 2020).

1.4. Definitions

The research project addressed the production of CO_2 emissions and the fuel consumption rate of modern internal combustion engines and aimed to develop an accurate computational fluid dynamics (CFD) model of an opposed-piston, two-stroke engine. Two-stroke engines produce more power than a conventional, four-stroke engine of the same displacement (Hooper et al., 2011). Some common terms that were utilized throughout this research are listed below, along with their respective definitions.

- Emissions
  - Emissions from internal combustion (IC) engines are mainly composed of carbon dioxide (CO_2, carbon monoxide (CO), unburnt hydrocarbons (HC), and nitric oxides (NO_x) (Fontaras et al., 2017).
- Power-to-weight ratio
  - The engine's power-to-weight ratio is defined as the ratio between the maximum rotary power output by the engine at the crankshaft and the engine's weight (Hooper et al., 2011).
- Fuel economy
  - Fuel economy is the distance a vehicle can travel per unit distance (Fontaras et al., 2017). In the US, fuel economy is measured in miles per gallon.
- Computational Fluid Dynamics (CFD)
  - Numerical simulation of flow physics utilizing conservation equations to numerically solve a flow problem (Changlu et al., 2015).
- Engine NVH
  - According to Hooper et al. (2011), "the noise, vibration, and harshness" (p. 1536) of engine operation.
- Scavenging Efficiency
  - Scavenging efficiency is defined as the final trapped fresh charge over the total cylinder charge (Mattarelli et al., 2017).

- Trapping Efficiency
    - Trapping efficiency is defined as the final trapped fresh charge over the final delivered fresh charge (Mattarelli et al., 2017).
- Bore
    - The bore is the cylinder's diameter in the engine (Zhenfeng et al., 2017).
- Stroke
    - The stroke is the linear distance traveled by each piston in the cylinder, from ODC to IDC (Zhengfeng et al., 2017).
- IDC
    - Inner dead center (IDC) is the limit of the pistons' motion at the center of the cylinder, much like top dead center (TDC) in a traditional engine (Zhengfeng et al., 2017).
- ODC
    - Outer dead center (ODC) is the limit of the pistons' motion at the ends of the cylinder, much like bottom dead center (BDC) in a traditional engine (Zhengfeng et al., 2017).

1.5. Assumptions

The proposed study made five fundamental assumptions.

- The CFD model assumed that the flow through the intake and exhaust manifolds is equally distributed to each transfer port and exhaust port on a multi-cylinder configuration.
- Another assumption was that the flow field within the cylinder is periodic. Assuming a periodic flow field allowed the CFD model to be cut into a slice of the full cylinder, saving computational resources and developing a finer mesh.
- It was also assumed that the intake ports' inlets are maintained at constant pressure by a supercharger.
- Similarly, the exhaust ports' outlets are maintained at atmospheric pressure without backpressure from an exhaust system.

1.6. Delimitations

The delimitations or scope of this research study were defined as follows. First, the proposed computational fluid dynamics (CFD) model was used to model and analyze the flow through one cylinder, opposed-piston combination. The one-cylinder delimitation was set to reduce computational time and made it feasible to complete the data collection and analysis phase within the given timeframe. Second, this study investigated the effect of two operating parameters on the engine's scavenging and trapping efficiency. The study analyzed the port angle and exhaust piston lead angle. Third, the research study examined the flow regime utilizing a hot flow (or combustion) analysis instead of a cold flow analysis.

1.7. Limitations

The limitations of the research study included time restrictions, computing resources, and funding restrictions. The limitations with the most impact on the research study were time and computing resources. The timeframe of this research project prevented investigating full-engine CFD models, as the development of an accurate full-engine model is extensive and would not allow sufficient time to complete data collection and analysis. Computing resources were another limitation of this experiment. Developing an accurate model for turbulent flow field analysis required many computational cells, especially within the boundary layer, where the flow field experiences large transients in velocity (Růžička, 2018). Since all model surfaces require a boundary layer for accurate modeling, the total size of the model needed to be reduced to allow for a reasonable computational time.

1.8. Summary

The aim of the research project was to analyze the effects of intake port geometry and exhaust piston lead angle on scavenging and trapping efficiencies. These efficiencies were evaluated in a computational fluid dynamics (CFD) model of an opposed-piston, two-stroke engine. Implementing such engines in modern vehicles could improve fuel economy and increase the power to weight ratio, both of which would reduce CO_2 emissions.

CHAPTER 2. REVIEW OF LITERATURE

2.1. Search Methodology

The proposed search methodology investigated the historical implementations and developments, the operating principles, and the current implementations and developments of opposed-piston, two-stroke engines.

2.1.1. Problem

The problem addressed by this project was the production of CO_2 emissions and the fuel consumption rate of modern internal combustion engines. The production of CO_2 emissions by internal combustion engines is one of the leading areas of research in powerplant development today (Dalla et al., 2018). The transportation sector is the leading contributor to CO_2 emissions (Environmental Protection Agency, 2020). Fuel economy is another important facet of modern internal combustion engines. Fontaras et al. (2017) stated within their research that fuel consumption is the performance metric that gets the most attention from the public, environmental, and consumer organizations. Reducing fuel consumption also reduces CO_2 emissions.

2.1.2. Search Strategy

Emissions, rotating mass, and power-to-weight ratio served as the main categories in the search strategy. First, emissions are related to CO_2 reduction, opposed-piston designs, two-stroke designs, computational fluid dynamics, and engine emissions performance (NO_x output and Hydrocarbon output). The rotating mass of an engine is related to engine stability, NVH (noise, vibration, and harshness), startup behavior, two-stroke design, opposed-piston design, and fuel economy (calculated through CFD). Finally, the power-to-weight ratio is related to two-stroke design, opposed-piston design, CFD, and fuel economy. This procedure left three concepts in the intersection of the three main circles: two-stroke, opposed-piston, and computational fluid dynamics. These three concepts were combined using the Boolean operator AND to generate search results. Figure 2. illustrates the search methodology process for the concepts listed above.

Figure 2.1. Search methodology Venn diagram.

After reviewing the gathered search materials from the Venn diagram search, four main literature topics were selected: history, operating principles, current prototypes, and current research.

2.2. History of Opposed-Piston, Two-Stroke Engines

During the development of internal combustion engines (1850-1900), single-cylinder engines were favored over multi-cylinder engines because of the lack of engine manufacturing tools in the 1800s (Pirault & Flint, 2010). The opposed piston concept (OP) was initially attractive because it eliminated the need to create a cylinder-head for the engine. Also, materials in the 1800s were not as strong as they are today. Therefore, the double stroke of the opposed-piston engine allowed smaller bores to be implemented, reducing the load on the crankshafts (Pirault & Flint, 2010).

Between 1900 and 1945, opposed-piston engines were installed in practical applications. Most installations were stationary or marine applications using diesel fuel (Pirault & Flint, 2010). Early engines had varying levels of success, and most utilized one crankshaft with long arms that connected the outer piston (Pirault & Flint, 2010). This particular design was largely unsuccessful.

2.3. Operating Principles

Opposed-piston, two-stroke engines operate like other two-stroke engine designs where the induction and compression events occur on the upward stroke while the power and exhaust (scavenging) events take place on the downward stroke. But, in opposed-piston engines, the cylinder head is eliminated, and two pistons moving towards and away from each other create the combustion volume (Pirault & Flint, 2010). This characteristic eliminates the heat losses from a cylinder head and reduces the number of moving parts in the engine, and introduces a few challenges.

The distinct advantages of opposed-piston, two-stroke engines include their higher specific output, specific torque, power density, and power-to-weight ratio (Pirault & Flint, 2010). Opposed-piston engines also offer lower heat-to-coolant ratios and higher reliability (Pirault & Flint, 2010). The raised specific output, torque, power density, and power-to-weight ratios of opposed-piston engines stem from their higher thermal efficiency and the two-stroke cycle. Since a two-stroke cycle ignites the fuel mixture every 360 degrees, it doubles the number of power strokes at a given rotational speed (Hooper et al., 2011). The doubled number of power strokes leads to approximately two times the power output per unit displacement over a four-stroke cycle.

Lower heat-to-coolant ratios and higher reliability originate from the reduced surface area of the combustion chamber exposed to the combustion event and fewer moving parts since a valvetrain and cylinder head are not implemented (Pirault & Flint, 2010).

The disadvantages of opposed-piston, two-stroke engines include top-ring scuffing problems, higher thermal loading of the piston and cylinder, and side injection (Pirault & Flint, 2010). Top-ring scuffing stems from the lack of load reversal on the piston in a two-stroke cycle (Pirault & Flint, 2010). This characteristic affects all two-stroke engines. Higher thermal loading of the piston and cylinder comes from more frequent combustion events and the absence of a cooling induction stroke (Pirault & Flint, 2010). Finally, controlling fuel impingement on the cylinder wall is difficult for side fuel injection. (Pirault & Flint, 2010).

2.4. Current Prototypes

The current prototype being developed for modern vehicles is the Achates Power opposed-piston, compression-ignition engine (Achates Power, 2018). Achates Power has developed a 2.7L, 3-cylinder opposed-piston, gasoline, compression-ignition engine for the F-150. Achates predicts their new engines will achieve 37 MPG in the F-150 with the capability of producing 270 hp and 480 lb-ft of torque (Achates Power, 2018).

2.5. Current Research

Four primary sectors of research exist in the opposed-piston, two-stroke engine field today. Piston design, as well as scavenge and transfer port design, are investigated to determine their effect on scavenging and trapping efficiency in a two-stroke engine. Hydrogen enrichment is another area of investigation for opposed-piston, two-stroke engines (along with other internal combustion engines) to examine combustion characteristics. Finally, studies have been conducted to determine accurate models for the scavenging action in uniflow engines.

Since opposed-piston engines do not have a cylinder head, the piston crown plays a critical role in shaping the combustion chamber of an opposed-piston engine. In 2015, Changlu, Fujun, Zhenfeng, and Shuanlu investigated the use of a flat piston and pitted piston using CFD. The pitted piston had a half dish cut out to facilitate scavenging in a non-uniform scavenging chamber. The pitted design of the piston saw significant improvements in combustion efficiency but did not improve scavenging or trapping efficiency. During 2019, Czyż, Siadkowska, and Sochaczewski conducted a similar experiment while investigating the model of an old aircraft opposed-piston engine. The researchers ran simulations for a flat piston crown and a near-spherical piston crown. Once again, the spherical combustion chamber provided better combustion efficiencies. These effects are most likely due to a sphere being the most theoretically efficient combustion chamber (Turns, 2012). Another study in 2015, conducted by Huo, Huang, and Hofbauer, studied the three different piston crown designs, each with a near-spherical center section and outgoing reliefs to allow for side injection of fuel. Huo, Huang, and Hofbauer found that the outgoing reliefs were vital as they facilitated the mixing of the side-injected fuel. These reliefs also prevented impingement of the fuel jet with the wall of the cylinders.

Another important aspect of current research is the investigation of the intake and exhaust port angles with respect to the cylinder. Angling the transfer and scavenging ports in a two-stroke engine supplies the required turbulent kinetic energy (TKE) to sustain efficient combustion (Changlu et al., 2015). During 2017, Mattarelli, Rinaldini, Savioli, Cantore, Warey, Potter, Gopalakrishnan, and Balestrino conducted a research study to evaluate the effects of inlet and exhaust port angle on scavenging and trapping efficiency. Mattarelli et al.'s research found that swirl angle, tilt angle, and exhaust piston lead angle were all critical to improving scavenging efficiency. Yet, their analysis made some simplifying assumptions to eliminate the combustion process from the model. Also during 2017, Zhenfeng, Yangang, Jun, Yaonan, Tiexiong, Yi, and Yuhang conducted a research study to develop an accurate numerical model for uniflow scavenging in an opposed-piston, two-stroke engine. During 2001, Betz published a dissertation analyzing mechanisms of flow mixing. One analysis he performed was on the tilt angle in an opposed-piston, two-stroke engine (the Jumo 205E). Betz found that a toroidal gas structure produced the best scavenging efficiencies in the cylinder. Kozal's thesis in 2017 studied the development of an opposed-piston, two-stroke engine for utility aircraft. Kozal found that the most influential operating parameter for such an engine was the exhaust piston lead angle, as it improved the scavenging efficiency of the engine. Thomas' thesis, in 2009, performed an in-depth investigation of a cam-plate opposed-piston engine. These cam-plate engines utilize a plate that the pistons ride on to create their motion profile rather than a crankshaft. While Thomas' thesis results do not directly apply to traditional opposed-piston engines, the developed CFD techniques were similar to the methods used for this research project.

Other areas of current research prevalent for opposed-piston, two-stroke engines today, but are not realized in this project's research, include mechanical efficiency of opposed-piston engines and free-piston opposed-piston engines. During 2011, Xu, S., Wang, Y., Zhu, T., Xu, T., and Tao, C. performed a research project which investigated the numerical analysis of a free-piston opposed-piston engine. Free-piston engines do not constrain the piston to a particular movement profile, allowing the piston to "free"-float in the cylinder. These engines are being investigated for stationary applications where their efficiencies can be realized, but it is difficult to transform their output into rotary motion. Morton, Riviere, and Geyer (2017) investigated the limits of mechanical efficiency in opposed-piston engines. Their research team found that due to the exhaust piston lead angle employed in these engines, the mechanical efficiency of the engine is limited. During the crankshaft's rotation, the pistons do not move with each other; therefore, at times, the pistons oppose each other's movement.

2.6. Literature Review Conclusions

Leading areas of today's research in opposed-piston, two-stroke engine design include combustion chamber design, intake (transfer) and exhaust port design, hydrogen enrichment, mechanical efficiency, and free-piston engine variants. The effects of geometric parameters on scavenging and trapping efficiency have been quantified for cold flow analyses and 1D hot flow analyses. However, the impact of changing engine parameters on a three-dimensional analysis, including combustion and full-cycle simulation, has not been fully realized. Therefore, the present work focuses on the effects of port geometry, chamber geometry, and exhaust piston lead angle on an engine model considering combustion and three-dimensional flow analysis.

CHAPTER 3. RESEARCH METHODOLOGY

3.1. Introduction

After reviewing the literature, the importance of scavenging and trapping efficiency in a two-stroke engine became apparent (Pirault & Flint, 2010; Mattarelli et al., 2017). Scavenging efficiency must be optimized in a two-stroke engine because it enables the engine to exhaust burned gases and draw in fresh charge. Trapping efficiency also must be optimized in a two-stroke engine because it describes the engine's ability to retain the fresh charge delivered to the cylinder. While a small amount of exhaust gas recirculation (EGR) is beneficial for NO_x emissions, the goal is to minimize the presence of burned gases and maximize the presence of unburned gases in the cylinder during each cycle. Creating this distribution of gases in the cylinder will lower CO emissions, raise engine efficiency, and raise power output from the engine (Mattarelli et al., 2017; Fontaras et al., 2017). In addition to increasing scavenging and trapping efficiencies, increasing turbulence within the cylinder is also essential to optimize fuel-air mixing (Changlu, 2015). The goal of the proposed methodology was to characterize the effects of transfer port geometry and exhaust piston lead angle on scavenging efficiency, trapping efficiency, and turbulence within the cylinder of an opposed-piston, two-stroke engine.

3.1.1. Research Type

The type of research exhibited by this research study was quasi-experimental. Since the investigated independent variables (port geometry and exhaust piston lead angle) were generated by the researcher rather than randomly selected. The selection of variable values was a design requirement of the experiment because there are limited ranges where the independent variables are physically sound. The chosen research design was treatment followed by observation, with the treatment being a numerical simulation utilizing the defining independent variables.

3.2. Population & Sample

The CFD model investigated the effects of intake port geometry on engine efficiencies and in-cylinder turbulence. Two variables defined the intake port geometry of the engine: swirl angle and tilt angle. The swirl angle is the angle between the port and the radial line of the cylinder. The tilt angle is the angle between the port and the BDC plane of the cylinder. Figure 3. illustrates the tilt and swirl angle.

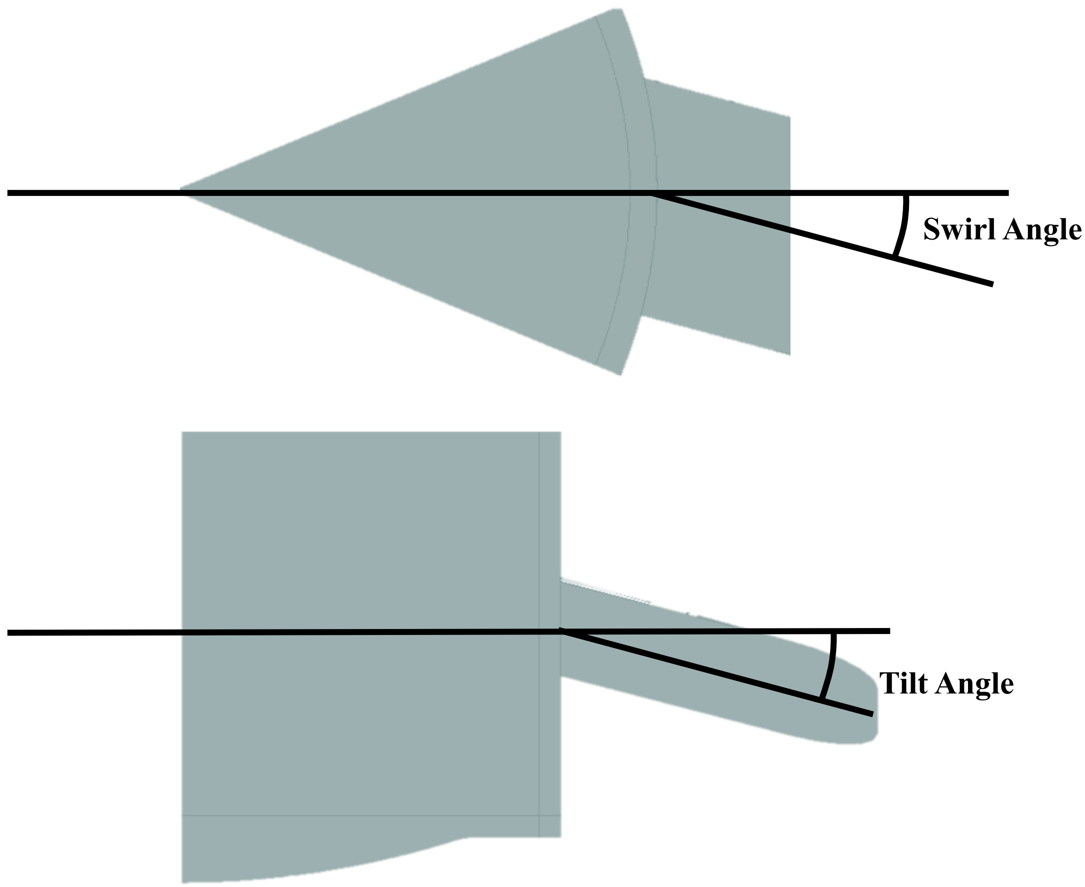

Figure 3.1. Tilt and swirl angle definitions for ports.

A parameter sweep of the port swirl angle and tilt angle was performed to answer the first research question. Table 3.1 illustrates the variable parameter sweeps for the first research question.

Table 3.1. Swirl and tilt angle parameter sweeps.

Tilt Angle Sweep			
Test Case	Swirl Angle, deg	Tilt Angle, deg	Lead Angle, deg
1	15	0	10
2	15	10	10
3	15	20	10
4	15	30	10
5	15	40	10
Swirl Angle Sweep			
Test Case	Swirl Angle, deg	Tilt Angle, deg	Lead Angle, deg
6	0	15	10
7	7.5	15	10
8	15	15	10
9	22.5	15	10
10	30	15	10

The selected samples for swirl and tilt angle are displayed in the two parameter sweeps from **Error! Reference source not found.**. The relevant populations that these samples were chosen from are 0-60 degrees for swirl and tilt angle. This population is produced from the physical limitations of creating ports that do not collide with one another.

The second research question investigated the effects of the exhaust piston lead angle on scavenging efficiency and trapping efficiency. The exhaust piston lead angle is the number of degrees the exhaust piston runs ahead of the intake piston (Mattarelli et al., 2017). Table 3.2 depicts the test run values for exhaust piston lead angle testing.

Table 3.2. Exhaust piston lead angle test cases.

Test Case	Swirl Angle, deg	Tilt Angle, deg	Lead Angle, deg
11	15	15	0
12	15	15	10
13	15	15	20
14	15	15	30

The sample for exhaust piston lead angle is given in Table 3.2. The population consists of physically plausible angles ranging from -180 to 180 degrees. Beyond the point of 30 degrees advanced, the exhaust ports will open too early.

3.3. Numerical Model

Throughout the research project, a CFD model was altered using geometric changes according to the independent variables. The developed model used an axisymmetric 45-degree section of the full piston-cylinder CAD model to reduce the number of computational elements required. The model was then meshed using ANSYS Mesher and simulated using ANSYS Fluent.

3.3.1. Geometry

The first step in developing the CFD model was to create a geometric model of the engine. A geometric model was developed utilizing CAD software with similarly scaled features from an opposed-piston, two-stroke aircraft engine from the 1930s and 1940s (Czyż, Siadkowska, & Sochaczewski, 2019). Table 3.3 illustrates the geometric model’s properties.

Table 3.3. Opposed-piston geometric model properties.

Engine Specification	Value	Unit
Bore	5.35	cm
Stroke	6	cm
Compression Ratio	12:1	-
Connecting Rod Length	12	cm
Crank Throw	3	cm
Number of Ports	8 Intake & 8 Exhaust	-
Port Area	0.787	cm^2

Once the geometric model's properties were established, a model of the cylinder-piston combination was developed. Complete and simplified geometric models are depicted in Figure 3.2. A periodic flow assumption was utilized within the cylinder to reduce the number of computational elements required to solve the flow problem.

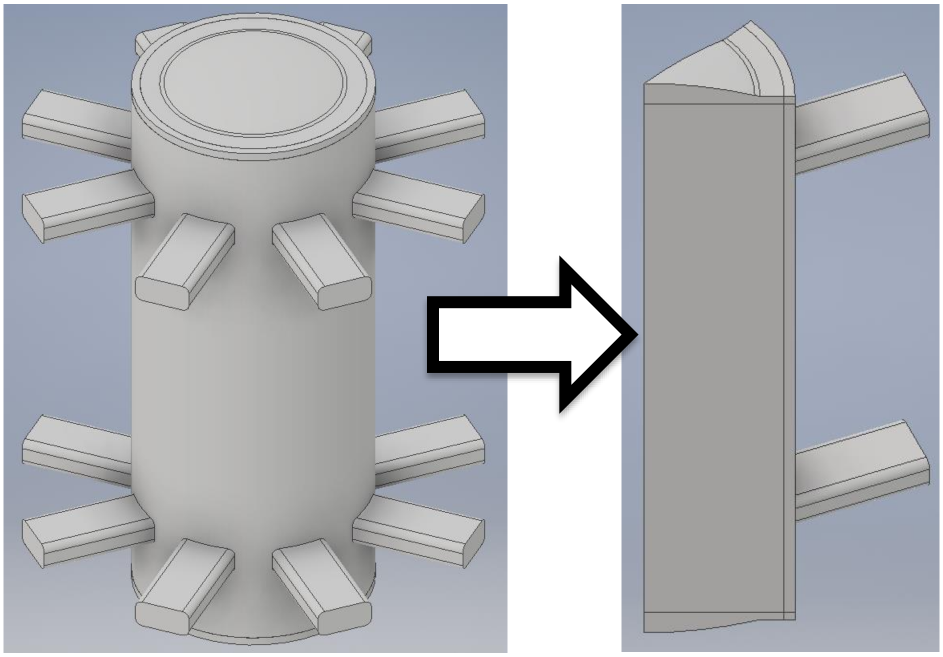

Figure 3.2. Axisymmetric simplification of geometric model.

3.3.2. Mesh

After developing a geometric model, the next step was the development of a computational mesh to set up the flow domain with computational elements. The transient analysis of an IC engine is unique because it requires a dynamic mesh to simulate the movement of the pistons within the cylinder.

Before establishing a dynamic mesh, the static mesh was developed to determine which domains contain structured or unstructured cells. Also, contact regions were set up between the ports and the cylinder wall to model the sliding port flow interaction. Unstructured meshes were utilized where possible since they simplified the process of creating an inflation layer to model turbulence. Figure 3.3 displays the computational mesh from each section of the model. The chamber volume and boundary layer were made up of hexahedral cells since the dynamic mesh required a structured mesh. The ports and piston dishes utilized an unstructured, tetrahedral mesh since this mesh easily conforms to complex geometry. Figure 3.4 illustrates the different cell sections created in the meshing program.

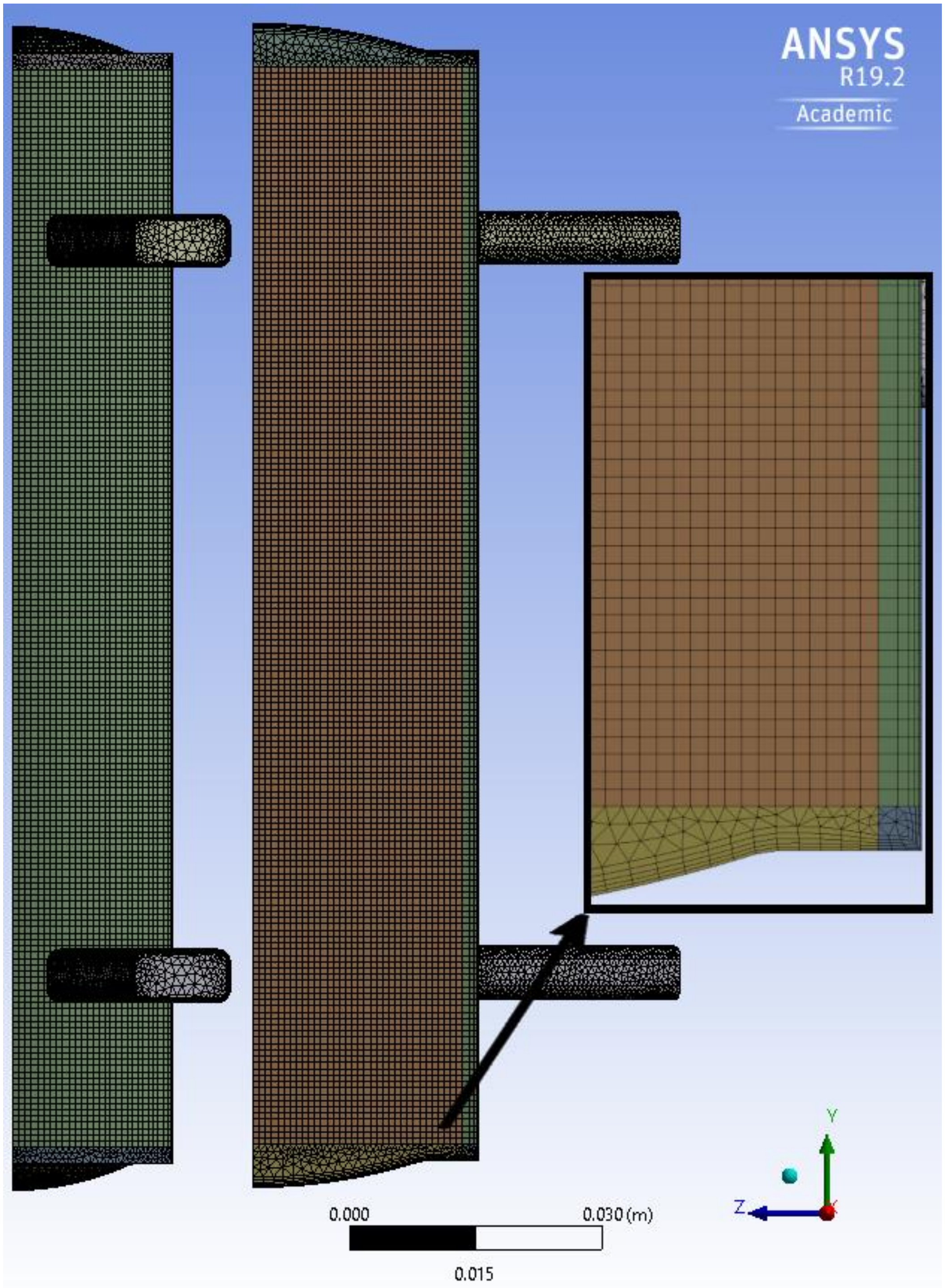

Figure 3.3. Computational mesh for opposed-piston, two-stroke engine. The model uses inflation layers, structured mesh, unstructured mesh, and cell bias to create a high quality mesh.

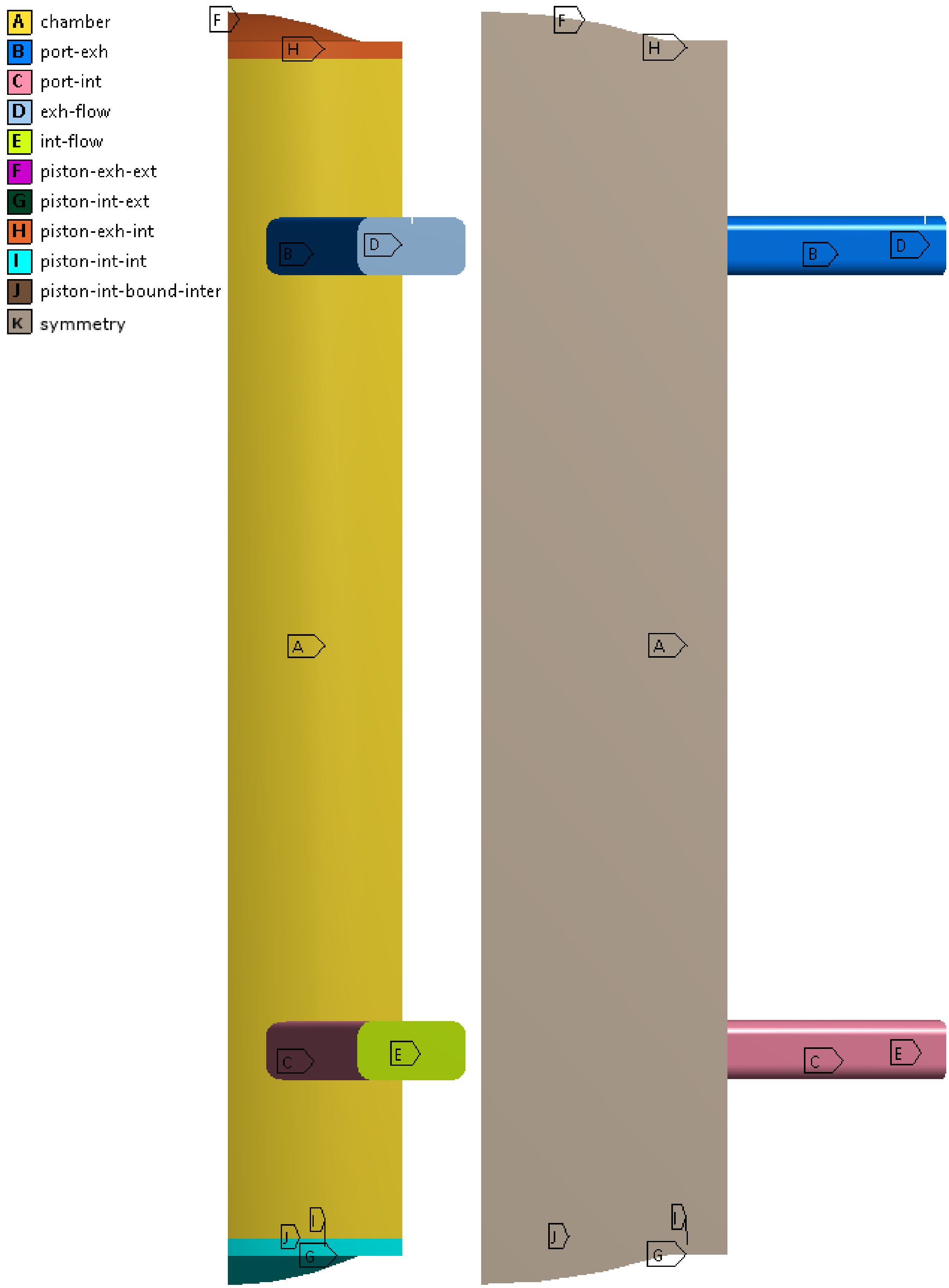

Figure 3.4. Named surfaces used for meshing.

3.3.2.1. Dynamic Mesh

The dynamic mesh in ANSYS Fluent was created using a piston profile generated with the following equations: r is the crank radius (m), a is the connecting rod length (m), l is the exhaust piston lead angle (degrees), and Θ is the crank angle from outer dead center (degrees).

$$\text{Intake Piston: } x = -r * \cos(\theta) - \sqrt{a^2 - r^2 * \sin(\theta)^2} + a + r \quad (3.1)$$

$$\text{Exhaust Piston: } x = -r * \cos(\theta + l) - \sqrt{a^2 - r^2 * \sin(\theta + l)^2} + a + r \quad (3.2)$$

The cylinder position x is defined as the distance from each piston's respective ODC position (m). Once the piston profiles were assigned, the Fluent model was set up to remove chamber cells as the pistons progressed towards inner dead center. Utilizing the properties fromTable 3.3, the piston profile for this project's dynamic mesh was created. Figure 3.5 (left) displays the motion of the pistons regarding the pistons' respective crankshaft for no exhaust piston lead. Figure 3.5 (right) shows the motion of the pistons with 15 degrees of exhaust piston lead.

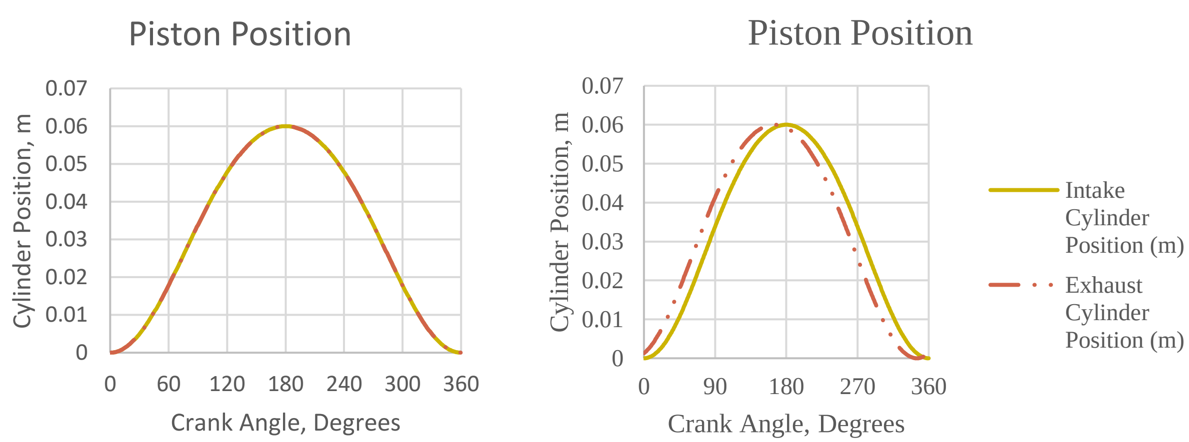

Figure 3.5. Piston position with no exhaust piston lead (left) and piston position with 15 degrees exhaust piston lead (right).

Once the piston profiles were generated, the dynamic mesh was set up in ANSYS Fluent. The dynamic mesh settings in Fluent require the operator to specify which areas of the mesh are deforming and which areas are rigid bodies moving through the flow field. The rigid bodies in a dynamic mesh do not experience mesh deformation during the simulation. Also, rigid bodies can be assigned a motion profile to control their movement during the transient simulation. Therefore, the piston and boundary interface mesh zones were set to rigid bodies with the piston profile obtained from Figure 3.5. The chamber mesh zone was defined as a deforming zone and utilized the layering mesh method. This dynamic mesh method removes mesh layers from the deforming zone in the chamber as the rigid body pistons traverse along their assigned motion profiles. Figure 3.6 (left) displays the mesh zones required for the deforming mesh in the chamber to operate properly.

Figure 3.6 (right) displays the dynamic mesh settings that set up the transient simulation time steps. These parameters were used to calculate the distance the pistons move during each time step. Crank shaft speed, crank radius, and connecting rod length were used to determine the change in piston position, while the crank shaft speed and crank angle step size were used to determine the duration of the time step. The crank shaft speed was set at 2000 RPM, the crank period was set to 360 degrees for the two-stroke cycle, the crank angle step size was set to 0.5 degrees, the crank radius was set to 3.0 cm, and the connecting rod length was set to 12 cm.

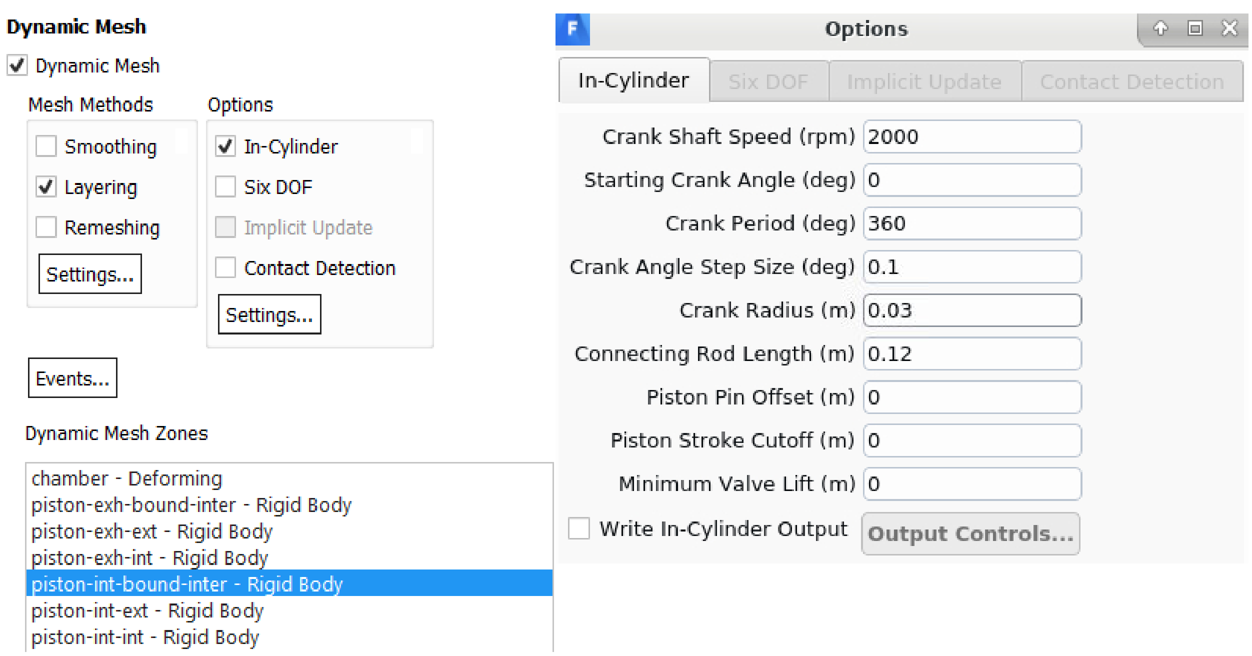

Figure 3.6. Dynamic mesh zones and their type (rigid body or deforming) (left) and dynamic mesh settings for speed of crank and piston motion (right).

3.3.3. Sliding Port Interfaces

Next, the sliding piston ports were modeled in ANSYS Fluent by setting up contact regions in the mesh model of the engine. Then, Fluent's mesh interfaces were utilized to interpolate the structured chamber element values from the unstructured port element values. Figure 3.7 illustrates the mesh interface setup for the opposed-piston model.

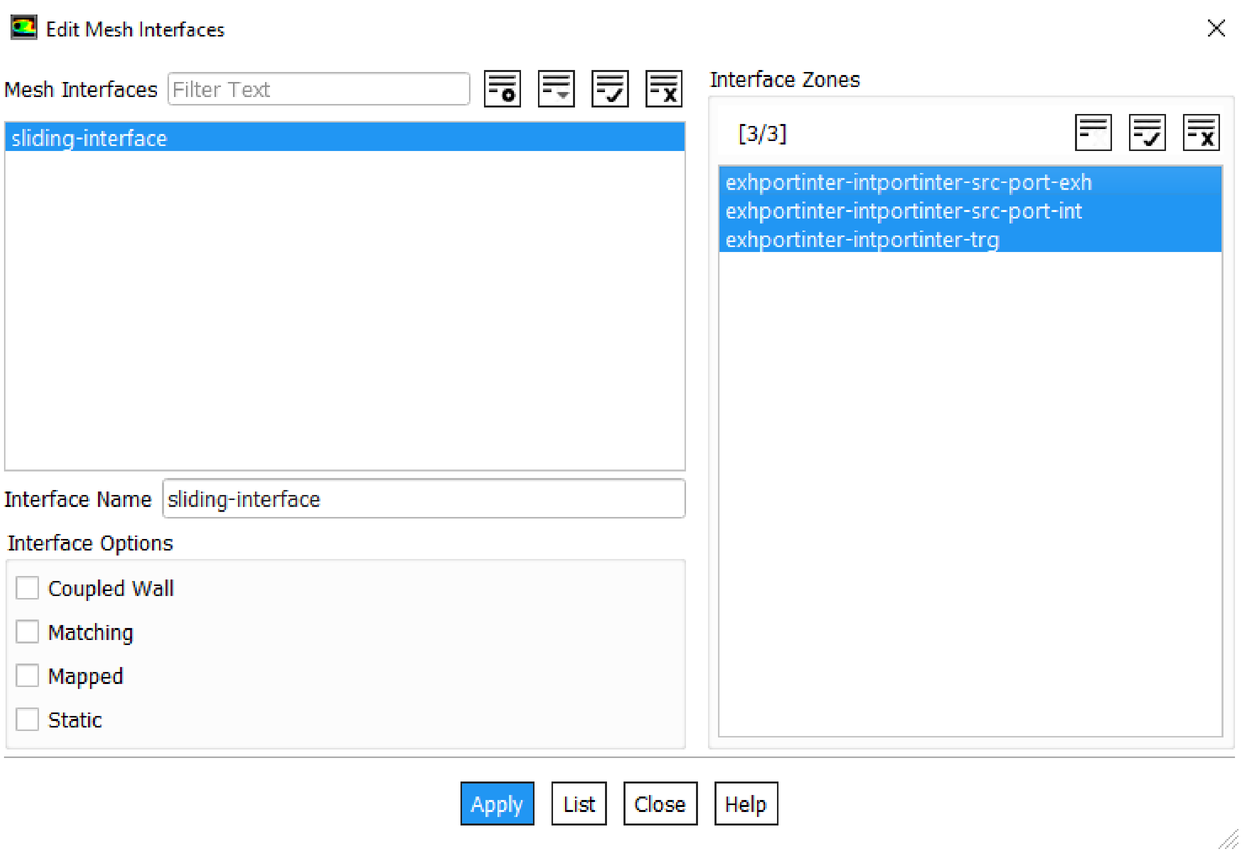

Figure 3.7. Sliding port interface setup for opposed-piston, two-stroke engine model.

Note the lack of interface options for the sliding interface. These interface options are used for thermal coupling (absence of fluid flow) and meshes that match at the interface (structured on both sides). This research project's sliding mesh utilized the standard mesh interface, which interpolates the values from the nodes on one side of the interface to the other. The standard setup works well for non-conformal meshes that support fluid flow.

3.3.4. Boundary Conditions

Finally, the CFD model required boundary conditions to set up the flow problem. Modern two-stroke, opposed-piston engines utilize superchargers, or blowers, to aid charge exchange and provide a favorable pressure gradient at the intake (or transfer) ports (Achates showcases, 2018). Therefore, the inlet port boundaries were considered as pressure inlets with a gauge pressure of one atmosphere. The exhaust port boundaries were considered as pressure outlets with a zero-gauge pressure. The chamber, piston, and port walls received a wall boundary condition with the no-slip condition for turbulence modeling. Finally, the inner chamber faces on either side of the 45-degree cut utilized periodic boundary conditions to set up the axisymmetric model. Figure 3.8 displays the boundary condition for each surface created in the mesh model (Figure 3.4). The *-interface-* surfaces were automatically generated by Fluent when the mesh interfaces for the ports were created.

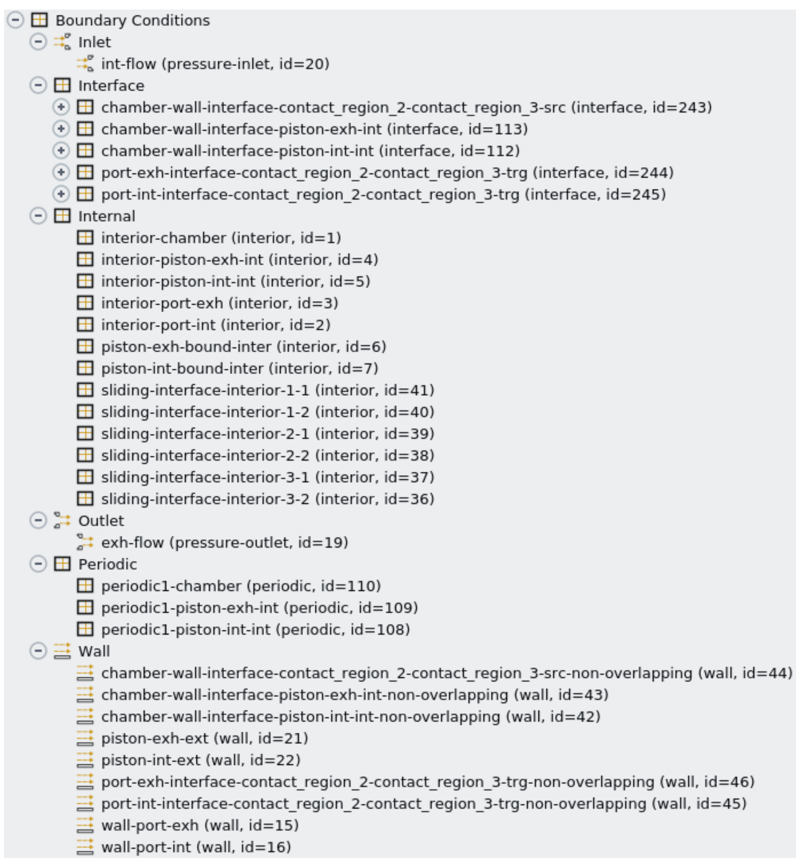

Figure 3.8. Boundary conditions for each surface of the opposed-piston, two-stroke engine model.

Once these design criteria were employed in the CFD model, the intake port and exhaust piston lead angle were modified to analyze two-stroke efficiencies.

3.3.5. Modeled Physics

When modeling a system numerically, it is crucial to select the appropriate equations to model the behavior of the system. The model setup for the opposed-piston engine utilized the standard momentum and continuity equations. The energy equation was also used because the fluid flow was modeled as an ideal gas and can be compressed, requiring another equation to fully describe the system. In an internal combustion engine, combustion and diffusion also occur. Therefore, appropriate models for combustion and diffusion were selected to model the engine's cycle accurately.

The addition of the combustion and diffusion equations to the numerical model required the use of a user-defined function as well. A user-defined function, or UDF, allows the user to utilize custom equations within the ANSYS Fluent solver. The UDF code, described in the following flow physics equations, is supplied in Appendix A.

The first section of the UDF calculated a heat release rate for the combustion simulation. Chemical kinetic models are available for combustion but are computationally expensive (Turns, 2012). Therefore, to reduce the computational expense and timeframe of the numerical model, the Wiebe function was selected. The Wiebe function models the burned mass fraction of the air-fuel mixture, which was then altered to create a heat input rate to the cylinder (Liu & Dumitrescu, 2019). Equations (3.3) and (3.4) define the Wiebe model as well as the heat input rate calculation.

$$x_b(\theta) = 1 - exp\left[-a\left(\frac{\theta - \theta_0}{\Delta\theta}\right)^{m+1}\right] \tag{3.3}$$

$$\frac{dQ_n}{d\theta} = \frac{dx_b(\theta)}{d\theta} m_{fuel} \cdot LHV_{fuel} \cdot \eta_{comb} - \cancel{\frac{dQ_{ht}}{d\theta}} \tag{3.4}$$

The variables for the Wiebe model are as follows:

- $x_b(\theta)$ is the burned mass fraction, θ is the crank angle (degrees), θ_0 is the start of combustion (SOC) crank angle (degrees), $\Delta\theta$ is the combustion duration (degrees), and a and m are experimentally determined parameters. For gasoline combustion engines a = 5 and m = 2

(Kirkpatrick, 1999). In addition, our engine simulation will utilize θ_0 = 160 degrees and $\Delta\theta$ = 30 degrees.

The variables for the heat release rate equation are as follows:

- Q_n is the heat release (J), m_{fuel} is the mass of the fuel in the cylinder (kg), LHV_{fuel} is the lower heating value of the fuel (J/kg), η_{comb} is the combustion efficiency, and Q_{ht} is the heat transfer rate to the surroundings during the combustion process (J) (Liu & Dumitrescu, 2019). For gasoline combustion, LHV_{fuel} = 43.4 MJ/kg and η_{comb} = 0.9 (Turns, 2012).

The heat transfer rate lost to the surroundings was modeled within ANSYS Fluent and therefore removed from the heat transfer rate equation (3.4). After removing the heat loss term, equation (3.4) was added to the UDF. The UDF then calculated a source term for Fluent by calculating the fuel mass in the cylinder and applying the Wiebe function. Once the source term was calculated, it was applied to the Fluent model, as shown in Figure 3.9.

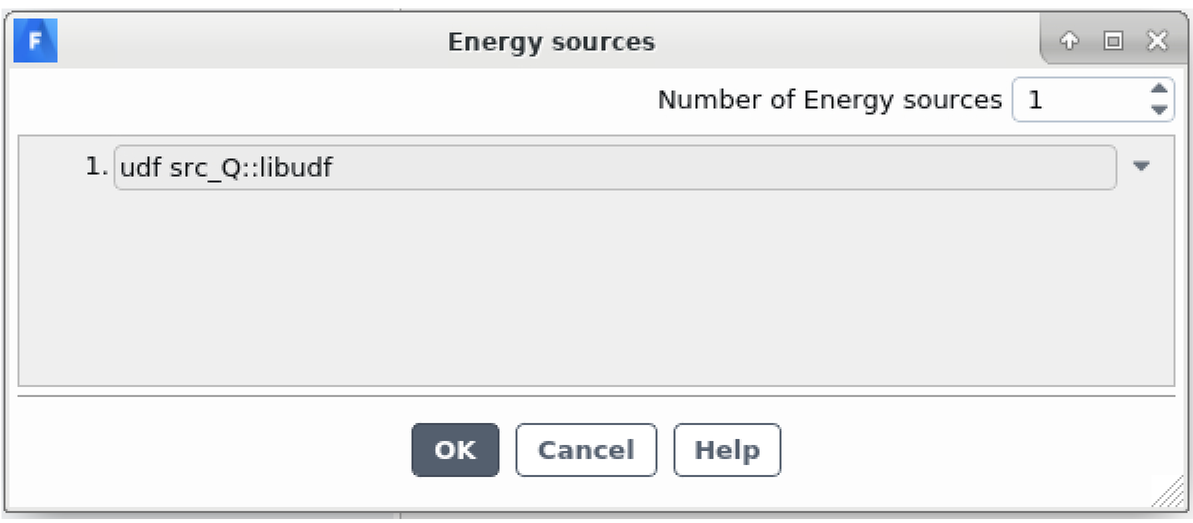

Figure 3.9. ANSYS Fluent dialog for hooking source terms into the numerical model.

The next section of the UDF calculated the binary diffusion coefficient for air and CO_2 to model the mass diffusion process when the unburned air charge enters the chamber. A low-pressure assumption can be made for the diffusion coefficient since the combustion products and the unburned air mix when the ports are open. This assumption allowed the use of the Hirschfelder equation (3.5) for the binary diffusion coefficient, D_{AB} (m^2/s) (Chen & Othmer, 1962).

$$D_{AB} = 0.018829 \sqrt{T^3 \left(\frac{1}{M_A} + \frac{1}{M_B}\right)} \frac{1}{p\sigma_{AB}^2 \Omega_{D,AB}} \tag{3.5}$$

$$\Omega_{D,AB} = \frac{1.06036}{T^{*0.15610}} + \frac{0.19300}{\exp(0.47635 \cdot T^*)} + \frac{1.03587}{\exp(1.52996 \cdot T^*)} + \frac{1.76474}{\exp(3.89411 \cdot T^*)} \tag{3.6}$$

$$T^* = \frac{T}{\left(\frac{\varepsilon_{AB}}{\kappa}\right)} \tag{3.7}$$

$$\frac{\varepsilon_{AB}}{\kappa} = \sqrt{\frac{\varepsilon_A}{\kappa}\frac{\varepsilon_B}{\kappa}} \tag{3.8}$$

$$\sigma_{AB} = \frac{1}{2}(\sigma_A + \sigma_B) \tag{3.9}$$

The variables for the Hirschfelder equation (3.5) are as follows:

- T is the temperature of the air (K), M_A is the molar mass of the first gas (g/mol), M_B is the molar mass of the second gas (g/mol), p is the pressure (Pa), σ_{AB} is a Lennard-Jones parameter (Å), and $\Omega_{D,AB}$ is the collision integral (Chen & Othmer, 1962).

The collision integral, $\Omega_{D,AB}$, is calculated using an equation (3.6) developed by Neufeld and recommended by Bird et al. (2007) in *Transport Phenomena*. The variables for the collision integral equation are as follows:

- T^* is non-dimensional temperature, T is the temperature of the air (K), and $\frac{\varepsilon_{AB}}{\kappa}$ is a Lennard-Jones parameter (K).

The values used throughout equations (3.5)-(3.9) were obtained from the Lennard-Jones tables in *Transport Phenomena* and are listed in Table 3.4 (Bird et al., 2007).

Table 3.4. List of gas constants used for diffusion calculations.

Variable Name	Value	Units
A	Air	-
B	CO_2	-
σ_A	3.55	Å
σ_B	4.49	Å
ε_A/κ	106	K
ε_B/κ	189	K
M_A	28.97	g/mol
M_B	44.01	g/mol

Once the diffusion coefficient was evaluated, Fluent applied the mass diffusion term to the mixing law. Figure 3.10 illustrates the location in Fluent where the mass diffusivity, or diffusion coefficient, was hooked into Fluent's internal diffusion equation.

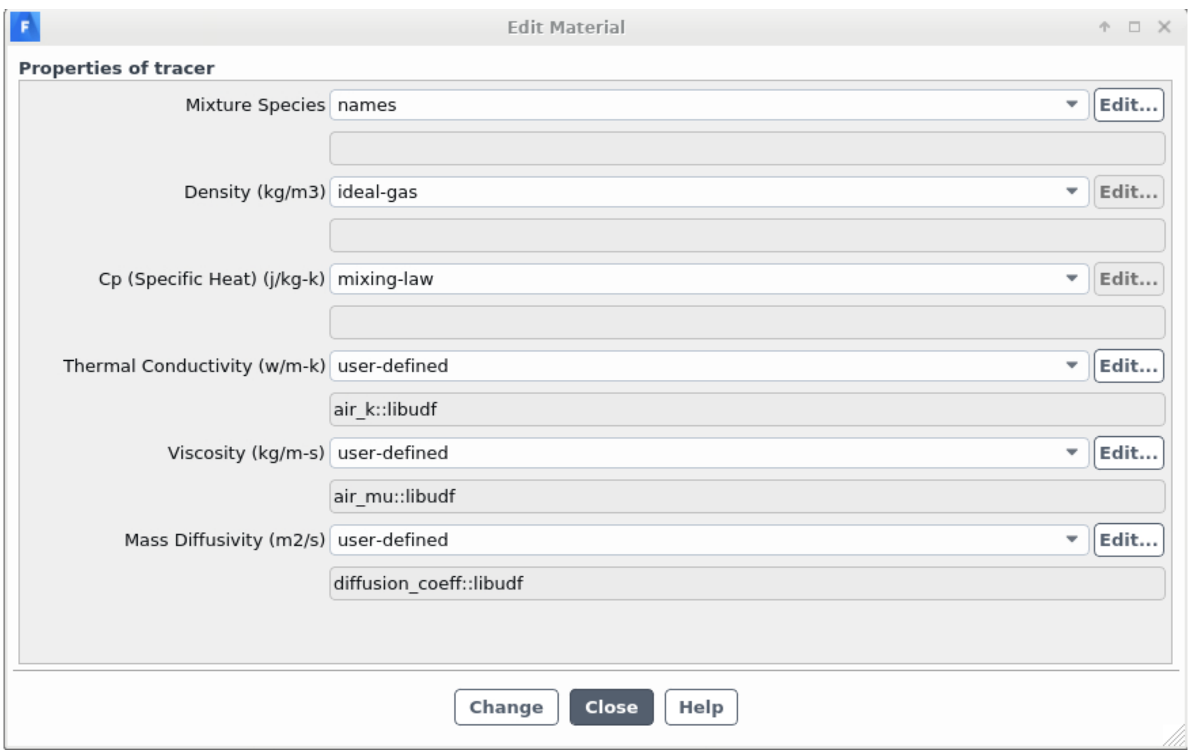

Figure 3.10. UDF hooking location for mass diffusivity, or diffusion coefficient.

In addition, the flow through an internal combustion engine is turbulent, so it is critical to select an appropriate turbulence model. The y^+ values were evaluated for the model's boundary layer cells to determine which turbulence model was most appropriate. The y^+ parameter is defined by equation (3.10) and was calculated by ANSYS Fluent during simulations (ANSYS, 2014).

$$y^+ = yu_\tau/\nu \tag{3.10}$$

$$u_\tau = \sqrt{\tau_{wall}/\rho} \tag{3.11}$$

Where y is the distance from the wall (m), u_τ is the friction velocity (m/s), ν is the kinematic viscosity (m^2/s), τ_{wall} is the wall shear stress (Pa), and ρ is the flow density (kg/m^3).

For the eighth test case y^+ values ranged from 3 to 108 while the intake and exhaust ports were closing. Therefore, a realizable κ-ε model was selected with scalable wall functions. The κ-ε model was selected because y^+ values were greater than 1, while scalable wall functions were selected because y^+ values were less than 30. For improved accuracy, the k-ω turbulence model could be used, but the first cell height must be reduced such that peak y^+ values are less than 1. Additional mesh cells would be required to achieve $y^+ < 1$, which would increase the computational expense. The k-ε turbulence model selected for this work provided a good balance of accuracy, relative to one-equation models, and computational cost, relative to the k-ω model.

3.4. Data Collection

During the data collection phase of the simulation, five parameters were considered: scavenging efficiency, trapping efficiency, normalized swirl circulation, normalized tumble circulation, and normalized turbulent kinetic energy. These parameters describe the engine's ability to expunge exhaust gases, retain fresh charges, and create turbulent energy in the combustion chamber.

3.4.1. Trapping Efficiency, Scavenging Efficiency, and Delivery Ratio

The equations for scavenging efficiency (3.12) and trapping efficiency (3.13) from Mattarelli et al.'s conference paper are shown below, where η_t is trapping efficiency (%) and η_s is scavenging efficiency (%). The defined fluid masses are represented as follows: mass of the final trapped fresh charge is m_t (kg), mass of the final delivered charge is m_d (kg), and total mass in the cylinder is m_c (kg).

$$\eta_t = m_t/m_d \tag{3.12}$$

$$\eta_s = m_t/m_c \tag{3.13}$$

The final delivered fresh charge value was calculated by integrating the mass flow at the transfer port during induction. The final total mass of the cylinder was extracted from ANSYS Fluent by summing the mass of each cell in the cylinder mesh. Finally, the trapped fresh charge was calculated by multiplying the total mass by the unburned gas mass fraction.

Another important metric for two-stroke engine performance is the delivery ratio (Mattarelli et al., 2017). Delivery ratio is represented in equation (3.14), where L is the delivery ratio, m_d is the mass of the delivered fresh charge (kg), and m_{ref} is the reference mass (kg).

$$L = m_d/m_{ref} \tag{3.14}$$

The reference mass is the product of ambient density and displacement volume. Once engine efficiencies were evaluated, the flow parameters of the engine cycle were calculated.

3.4.2. Swirl and Tumble

The flow parameters calculated during the data collection process included swirl circulation and tumble circulation. First, the equation for circulation was determined from the *Fluid mechanics* textbook (Kundu et al., 2004, p. 60). The initial equation for circulation is given in (3.15).

$$C \equiv \oint U \cdot dl \tag{3.15}$$

Where C is the circulation (m^2/s), U is the velocity (m/s), and l is the position (m) along the contour where circulation is being evaluated. Stokes' theorem was then used to create the identity in (3.16).

$$\oint U \cdot dl = \iint_A (\nabla \times U) \cdot ndA \equiv C \tag{3.16}$$

$(\nabla \times U)$, or the curl of the velocity field is equal to the vorticity field. Therefore, (3.16) states that the normal component of vorticity integrated over the area enclosed by the contour is equal to the circulation around the contour.

Applying (3.16) to the numerical model determines the integral (3.17) for swirl circulation and the integral (3.18) for tumble circulation.

$$C_{swirl} = \iint_A y - vorticity\ dA_{XZ} \tag{3.17}$$

$$C_{tumble} = \iint_A x - vorticity\ dA_{YZ} \tag{3.18}$$

Swirl circulation about the cylinder's XZ-contour is the integral of y-vorticity over the XZ-plane at inner dead center. Tumble circulation about the cylinder's YZ-contour is the integral of x-vorticity over the YZ-plane. Figure 3.11 illustrates examples of vorticity fields that are integrated into circulation values.

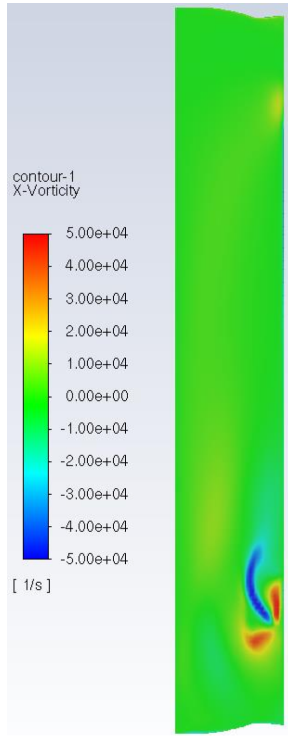

Figure 3.11. Tumble vorticity within the YZ-contour of the cylinder.

Also, when analyzing flow parameters in a system that is commonly scaled up and down, it is beneficial to normalize the parameters using characteristic dimensions and operating parameters. The mean piston speed (3.19) was used to normalize turbulent kinetic energy, swirl circulation, and tumble circulation where r is the crank radius (m), ω_{crank} is the crank speed (rpm), and V_{mean} is the mean piston speed (m/s). In addition to a velocity, the circulation values required a characteristic length for normalization. For this analysis, bore diameter (d_{bore} (m)) was selected. Equations (3.20)-(3.22) describe the normalized output parameters.

$$V_{mean} = 4r * \omega_{crank} * \frac{1\ min}{60\ s} \tag{3.19}$$

$$\widetilde{TKE} = \frac{TKE}{V_{mean}^2} \tag{3.20}$$

$$\widetilde{C_{swirl}} = \frac{C_{swirl}}{V_{mean} * d_{bore}} \tag{3.21}$$

$$\widetilde{C_{tumble}} = \frac{C_{tumble}}{V_{mean} * d_{bore}} \qquad (3.22)$$

Where $\widetilde{TKE}$, $\widetilde{C_{swirl}}$, and $\widetilde{C_{tumble}}$ are the normalized parameters, C_{swirl} is the swirl circulation, and C_{tumble} is the tumble circulation. Once these output parameters were gathered and normalized for each test case, an analysis took place to determine if the input parameters impacted each output parameter.

3.5. Analysis

According to Saltelli et al. (2019), a common method of analyzing numerical models is to perform a sensitivity analysis (SA) on the input and output parameters of the numerical model. Sensitivity analyses are a form of comparative analysis where the relationship between two or more variables can be determined (Saltelli et al., 2019).

Both research questions in this study compared the effect of three continuous input parameters on five continuous output parameters. When conducting a sensitivity analysis, the researcher ideally investigates the entire input space (Saltelli et al., 2008). The input space consists of the entire range of model input combinations. For example, when combining the three parameter sweeps of the engine model, 100 possible input parameter combinations make up the input space. Optimally, all 100 models would be included in a variance-based analysis to determine the significance of transfer port geometry and exhaust piston lead angle (Saltelli et al., 2008). Figure 3.12 illustrates the complete input space with a unique test case at every point in the cube.

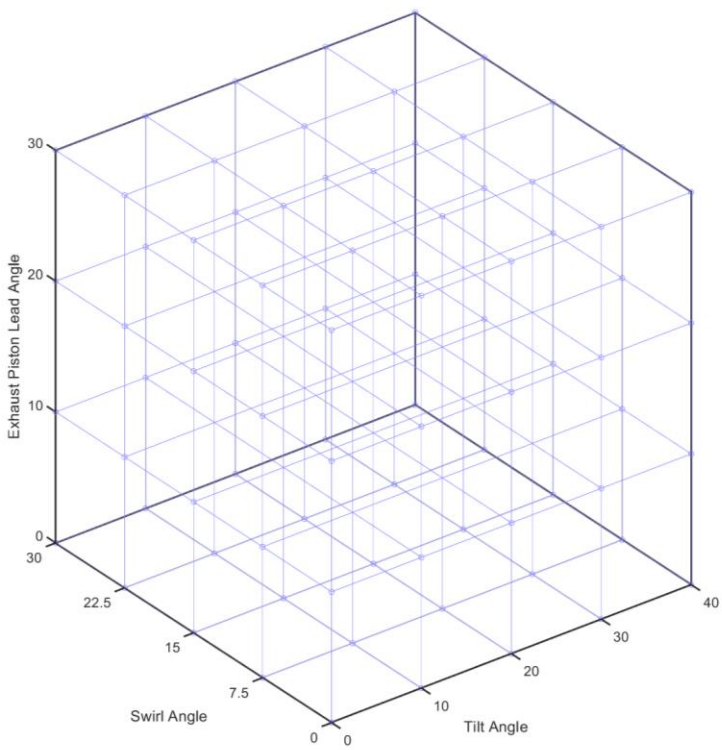

Figure 3.12. Input space representation regarding the parameter sweeps for tilt angle, swirl angle, and exhaust piston lead angle.

Since the CFD model required 12-16 hours to run, reducing the number of test cases needed for the analysis was crucial. The analytic method of modifying one input parameter while holding other input parameters constant is known as a one-at-a-time (OAT) analysis (Saltelli et al., 2019). A visual representation of the OAT input space is shown in Figure 3.13, and the input space is reduced to 14 test cases along the three parameter sweeps (black trajectories). Once the input parameter trajectories were determined, the one-at-a-time method was used to determine each input parameter's influence on the model's output using a sensitivity coefficient.

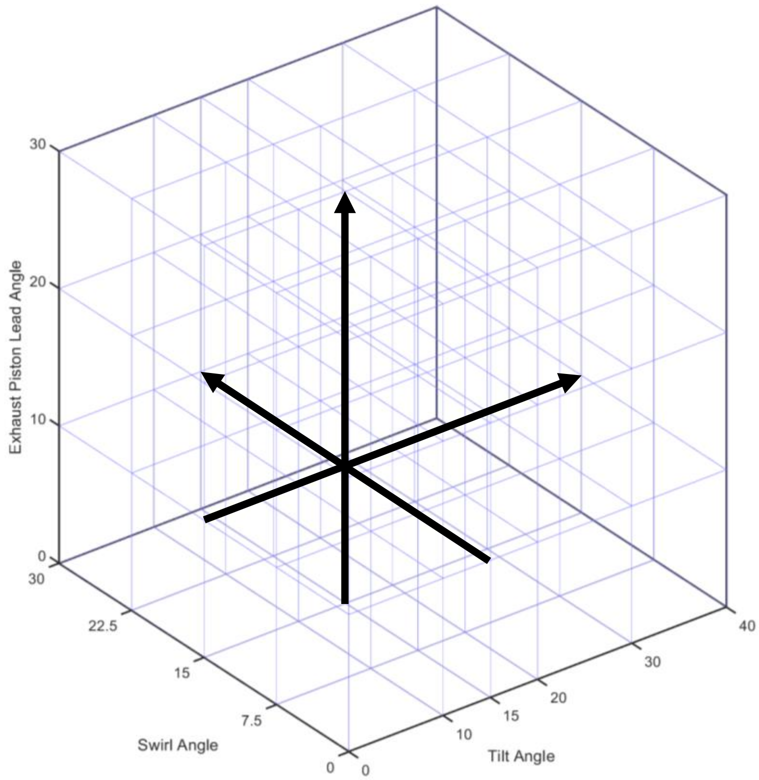

Figure 3.13. Parameter sweeps through the input space for tilt angle, swirl angle, and exhaust piston lead angle.

The first research question addressed the importance of transfer and scavenge port geometry for scavenging efficiency, trapping efficiency, and internal turbulence in an opposed-piston, two-stroke engine. While this has been characterized in the literature for traditional two-stroke engines, the effects on uniflow, opposed-piston engines are still being analyzed (Mattarelli et al., 2017). The input parameters for the first research question were swirl and tilt angle, while the output parameters were scavenging efficiency, trapping efficiency, normalized swirl circulation, normalized tumble circulation, and normalized turbulent kinetic energy.

The second research question addressed the importance of exhaust piston lead angle in improving the scavenging efficiency, trapping efficiency, and internal turbulence. The input parameter for this research question was exhaust piston lead angle, while the output parameters were scavenging efficiency, trapping efficiency, normalized swirl circulation, normalized tumble circulation, and normalized turbulent kinetic energy.

Since the research questions compared the output of the model while modifying swirl and tilt angle and exhaust piston lead angle, a significance index was used to compare the effect of transfer port geometry and exhaust piston lead angle (Saltelli et al., 2008). For the engine model data, the sensitivity coefficient was considered to characterize the effect of each input parameter on each output parameter. The sensitivity coefficient normalizes the partial derivative of the output parameter with respect to an input parameter. The equation for the sensitivity coefficient of each test case is given by (3.23). Due to the effects of nonlinearity, the maximum sensitivity coefficient, given by (3.24), was considered for the research project. The maximum coefficient reports the most significant sensitivity coefficient obtained from each input parameter sweep.

$$\hat{S}_i = \left|\frac{\partial Y_i}{\partial X_i}\frac{X_i}{Y_i}\right| \tag{3.23}$$

$$S = \max_{\mathrm{i}}\left(\hat{S}_i\right) \tag{3.24}$$

Where S is the maximum sensitivity coefficient for each input parameter sweep, $\hat{S}_i$ is the sensitivity coefficient for each test case, Y_i is the test case output parameter, and X_i is the test case input parameter.

Once the sensitivity coefficient was defined, the method of determining the partial derivative was developed. Since nonlinear effects were expected from the data, the central difference method was selected for the partial derivative. The central difference method is a second-order approximation which is why it was chosen for the interior points. At the boundaries, the exterior points utilized one-sided difference methods.

Once the partial derivative and sensitivity coefficient were calculated, the effect of tilt angle, swirl angle, and exhaust piston lead angle could be evaluated for scavenging efficiency, trapping efficiency, normalized swirl circulation, normalized tumble circulation, and normalized turbulent kinetic energy.

3.6. Reliability and Validity

The reliability, or model consistency, was verified using a grid-refinement CFD convergence study. The grid-refinement CFD study was performed by reducing the size of the computational elements in the mesh and comparing the outputs between the coarse, medium, and fine mesh. If the outputs matched, the mesh was said to have converged; otherwise, the mesh was refined again until convergence occurred.

3.6.1. Weaknesses of Methodology

Some specific weaknesses of the developed methodology for this research project included:

- lack of experimental validation,
- model generalizability,
- and a partial description of the entire system.

The lack of experimental validation stemmed from the undersupply of time and monetary resources to develop a piston-cylinder test set up to perform experimental validations for the numerical model. Model generalizability is a weakness of any numerical simulation because significantly changing the geometry requires additional grid-refinement studies to verify the reliability of the developed mesh and simulation results (Stern et al., 2001). Finally, this numerical model only partially described the opposed-piston engine system. Operational engines would require intake and exhaust manifolds as well as additional piston-cylinder combinations in transport applications.

CHAPTER 4. RESULTS

A grid independence study was conducted for Test Case #1 from Table 3.1, which had geometric parameters of: swirl angle = 0°, tilt angle = 15°, and exhaust piston lead angle = 10°. Simulations were conducted using coarse, medium, and fine meshes. The grid independence study showed that the medium mesh was sufficiently refined. Each subsequent test case from the test matrix, in **Error! Reference source not found.** and Table 3.2, was conducted using the same mesh sizing constraints as the medium mesh for Test Case #1.

The output variables and the collection location for each variable were as follows:

- air mass (kg) in the cylinder,
- unburned air mass (kg) in the cylinder,
- volume average mass fraction of burned air in the cylinder,
- volume average static pressure (Pa) in the cylinder,
- volume average static temperature (K) in the cylinder,
- volume average diffusion coefficient (m^2/s) in the cylinder,
- volume average combustion heat generation rate (J/deg) in the cylinder,
- volume average combustion heat input (J) into the cylinder,
- mass flow rate (kg/s) through the exhaust port,
- mass flow rate (kg/s) through the intake port,
- swirl circulation (m^2/s) at IDC,
- tumble circulation (m^2/s) bisecting the ports and cylinder,
- tumble circulation (m^2/s) bisecting only the cylinder,
- and volume average turbulent kinetic energy (m^2/s^2), or TKE, in the cylinder.

After the data parameters were collected, the normalized swirl circulation (equation (3.21)), normalized tumble circulation (equation (3.22)), and normalized TKE (equation (3.20)) were calculated. Also, the trapping (equation (3.12)) and scavenging efficiencies (equation (3.13)) were calculated.

4.1. Grid Independence Study

To perform a grid convergence study, a coarse, medium, and fine mesh were constructed of the cylinder model, Test Case #1. The element sizes for each mesh designation were as follows: coarse mesh – 0.001 m, medium mesh – 0.00075 m, and fine mesh 0.0005 m. Simulations were conducted for each mesh refinement. Then, integral flow parameters and instantaneous flow parameters were analyzed.

4.1.1. Integral Flow Parameters

Integral flow parameters included the scavenging efficiency, trapping efficiency, and delivery ratio. These values were calculated for each mesh and the relative percent changes are tabulated in **Error! Reference source not found.**able 4.1

Table 4.1. Percent change in engine efficiencies due to mesh refinement.

Mesh Transition	Scavenging Efficiency Change, %	Trapping Efficiency Change, %	Delivery Ratio Change, %
Coarse to Medium	0.04	-0.56	1.54
Medium to Fine	0.03	0.21	0.52

Data from **Error! Reference source not found.** confirmed the convergence of the mesh for the ANSYS Fluent cylinder model. For the coarse mesh, scavenging efficiency changed 0.036%, trapping efficiency changed -0.56%, and delivery ratio changed 1.54% when compared to the medium mesh. Therefore, the delivery ratio was the controlling parameter for convergence. For the medium to fine mesh transition, delivery ratio changed by 0.52%. Thus, the medium mesh was considered sufficiently refined. Subsequent simulations used similar mesh sizing constraints to achieve a level of refinement similar to the medium mesh for Test Case #1.

Another significant trend to consider during a grid convergence study is that the convergence curves exhibit an asymptotic behavior (Stern et al., 2001). Scavenging efficiency and delivery ratio exhibited asymptotic behavior while trapping efficiency showed an oscillatory convergence due to its sign changing. While the oscillatory behavior revealed an instability in the sign of the trapping efficiency error, the magnitude declined for the medium mesh to fine mesh transition. Therefore, the oscillatory function was confined by an asymptotic envelope. The asymptotic envelope confirmed the convergent behavior of trapping efficiency (Stern et al., 2001).

4.1.2. Instantaneous Flow Parameters

Instantaneous flow parameters included: normalized swirl circulation, normalized tumble circulation, and normalized TKE. These instantaneous flow parameters were considered, in addition to the integral parameters, during the grid convergence study. The trends of the instantaneous parameters were considered instead of a strict grid convergence study due to large impulses during port opening and closing. These port events created strong transients, which made instantaneous flow parameters unsuitable for convergence analysis.

Figure 4.1 displays the normalized TKE values for each grid size; coarse, medium, and fine. Peak normalized TKE values are experienced 20 degree after the intake ports open (320-, 680-, and 1040-degrees crank angle). For the grid convergence study, peak normalized turbulent kinetic energy values range from 174.6 for the medium mesh to 177.7 for the coarse mesh. A second observation point is during exhaust port closing, or EPC, at 778 degrees. Normalized TKE ranged from 30.1 to 31.33 at EPC.

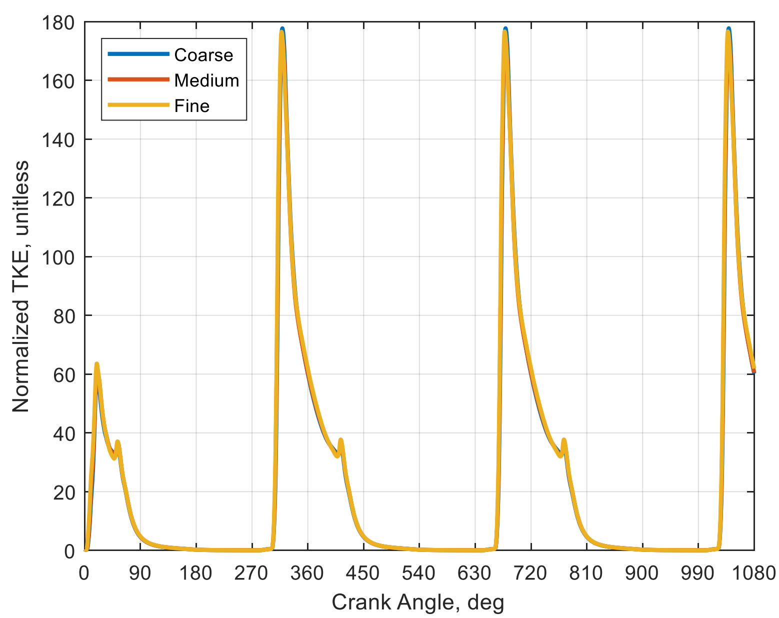

Figure 4.1. Instantaneous, normalized turbulent kinetic energy for coarse, medium, and fine meshes applied to Test Case #1.

Figure 4.2 illustrates the normalized swirl circulation for each grid size. Since the grid convergence study was performed for a test case with zero swirl angle, the typical peaks at intake port opening (IPO) and exhaust port closing (EPC) were not present. Also, normalized swirl circulation values did not appear to converge unless a more reasonable axis range was used. Therefore, two scales were used to display the normalized swirl values for the grid convergence study. The dotted lines represent the solid lines magnified forty times. The cause of the oscillations shown in the normalized swirl circulation during the time the piston ports are open was the periodic boundary condition. At zero swirl angle, the incoming flow is divided across the central axis of the cylinder, making periodic flow modeling difficult, compared to the test cases which incorporated swirl angle.

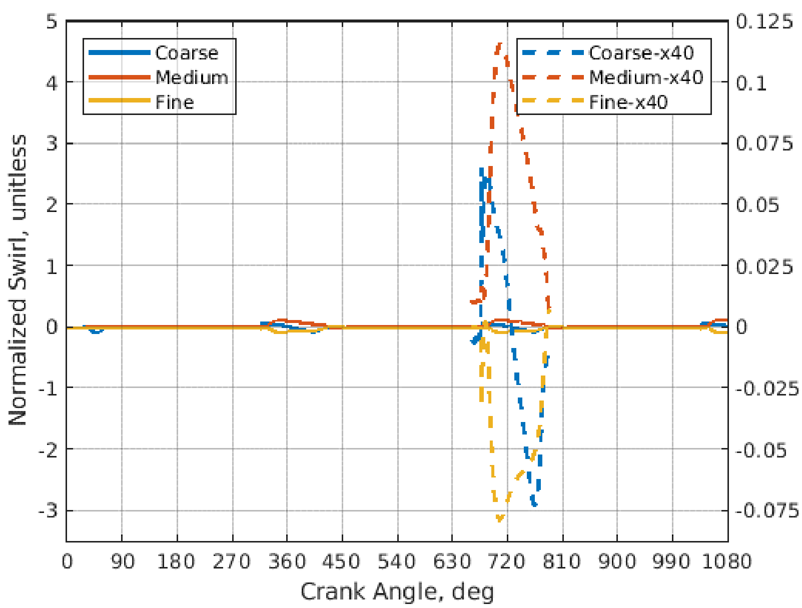

Figure 4.2. Instantaneous, normalized swirl circulation for coarse, medium, and fine meshes applied to Test Case #1.

Figure 4.3 shows the normalized tumble circulation for each grid size. Normalized tumble circulation, like normalized TKE, peaked 20 degrees after IPO with values ranging from -102.9 for the medium mesh and -106.5 for the coarse mesh. The second local maximum also occurred at EPC, with values ranging from -27.09 for the coarse mesh and -29.65 for the fine mesh.

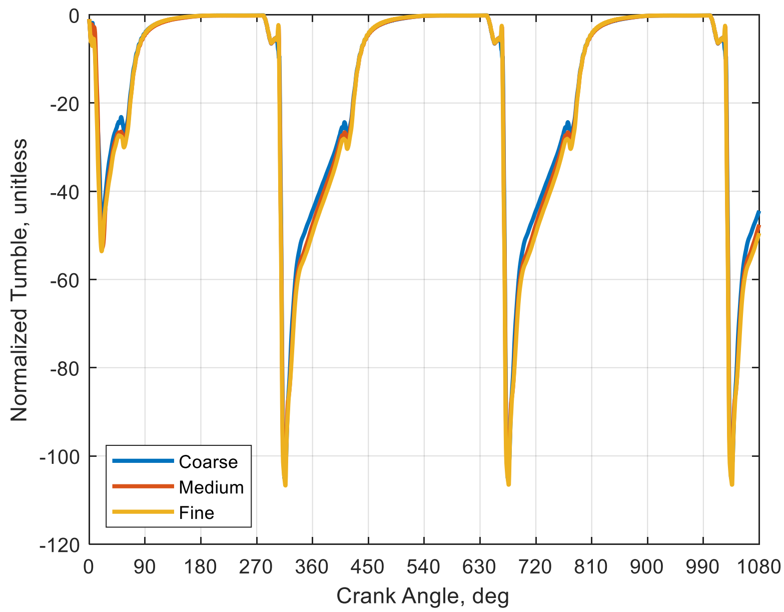

Figure 4.3. Instantaneous, normalized tumble circulation for coarse, medium, and fine meshes applied to Test Case #1.

4.2. Experimental Results

Table 4.2 displays the five output parameters considered when answering the thesis research questions. The first ten test cases investigated the effect of transfer port geometry on the output parameters. In comparison, the last four test cases investigated the impact of exhaust piston lead angle on the output parameters. The tilt angle, swirl angle, and exhaust piston lead angle for the test cases referenced in Table 4.2 are listed in Table 3.1 for transfer port geometry and Table 3.2 for exhaust piston lead angle.

Table 4.2 List of numerical model results (refer to Tables 3.1 and Table 3.2 for test case information).

Test Case	Scavenging Efficiency, %	Trapping Efficiency, %	Normalized Swirl Circulation	Normalized Tumble Circulation	Normalized TKE
1	99.83	23.49	3.73	15.05	36.87
2	99.87	23.11	3.30	18.86	33.07
3	99.94	22.97	3.46	18.20	32.19
4	99.96	22.80	3.24	13.97	34.67
5	99.82	22.52	2.82	5.31	42.83
6	99.89	23.09	0.01	-28.52	31.07
7	99.90	22.79	2.66	-22.57	32.96
8	99.92	23.12	3.49	21.11	32.37
9	99.67	23.07	3.62	20.42	26.94
10	99.31	22.94	4.45	19.15	22.69
11	99.91	17.67	2.93	10.82	14.20
12	99.92	23.12	3.49	21.11	32.37
13	99.83	26.06	3.69	23.91	32.89
14	99.73	25.69	3.72	20.41	33.68

Also, normalized swirl circulation, normalized tumble circulation, and normalized TKE were dependent on crank angle. Therefore, normalized circulation and normalized TKE values were evaluated where each parameter was most influential. According to Changlu et al. (2015), the circulation and TKE in the cylinder are crucial at exhaust port closing (EPC). Following EPC, turbulent kinetic energy is responsible for accelerating air-fuel mixing from a micro perspective (Changlu et al., 2015). In contrast, swirl and tumble circulation contribute to the formation of a homogenous air-fuel charge from a macro perspective (Changlu et al., 2015). The exhaust port closing crank angles of each test case are given in Table 4.3.

Table 4.3. Crank angle where exhaust port closing occurs for each test case.

Test Case	Exhaust Port Close Crank Angle, degrees
1-10	778
11	768
12	778
13	788
14	798

One definitive takeaway from this set of experimental results was that blowers on two-stroke engines effectively boost scavenging efficiency. Regardless of transfer port geometry and exhaust piston lead angle, the scavenging efficiency remained above 99%.

4.3. Parameter Sweep Comparisons

After developing and verifying the grid convergence of the medium grid size for the mesh, the remaining test cases were run to gather variable data. The first five test cases considered changes in transfer port tilt angle. The goal of altering the tilt angle was to influence the tumble circulation within the cylinder to increase turbulent kinetic energy (TKE). The second five test cases considered changes in transfer port swirl angle. The goal of changing the swirl angle was to influence the swirl circulation within the cylinder to boost TKE. The last four test cases realized changes in exhaust piston lead angle to alter port timing. The goal of modifying the lead angle was to investigate port timing's effect on engine efficiencies.

Figure 4.4 illustrates an example of the flow parameter plots used in the parameter sweep comparisons and marks the important events that occur in the full cycle plot (upper) and the combustion plot (lower).

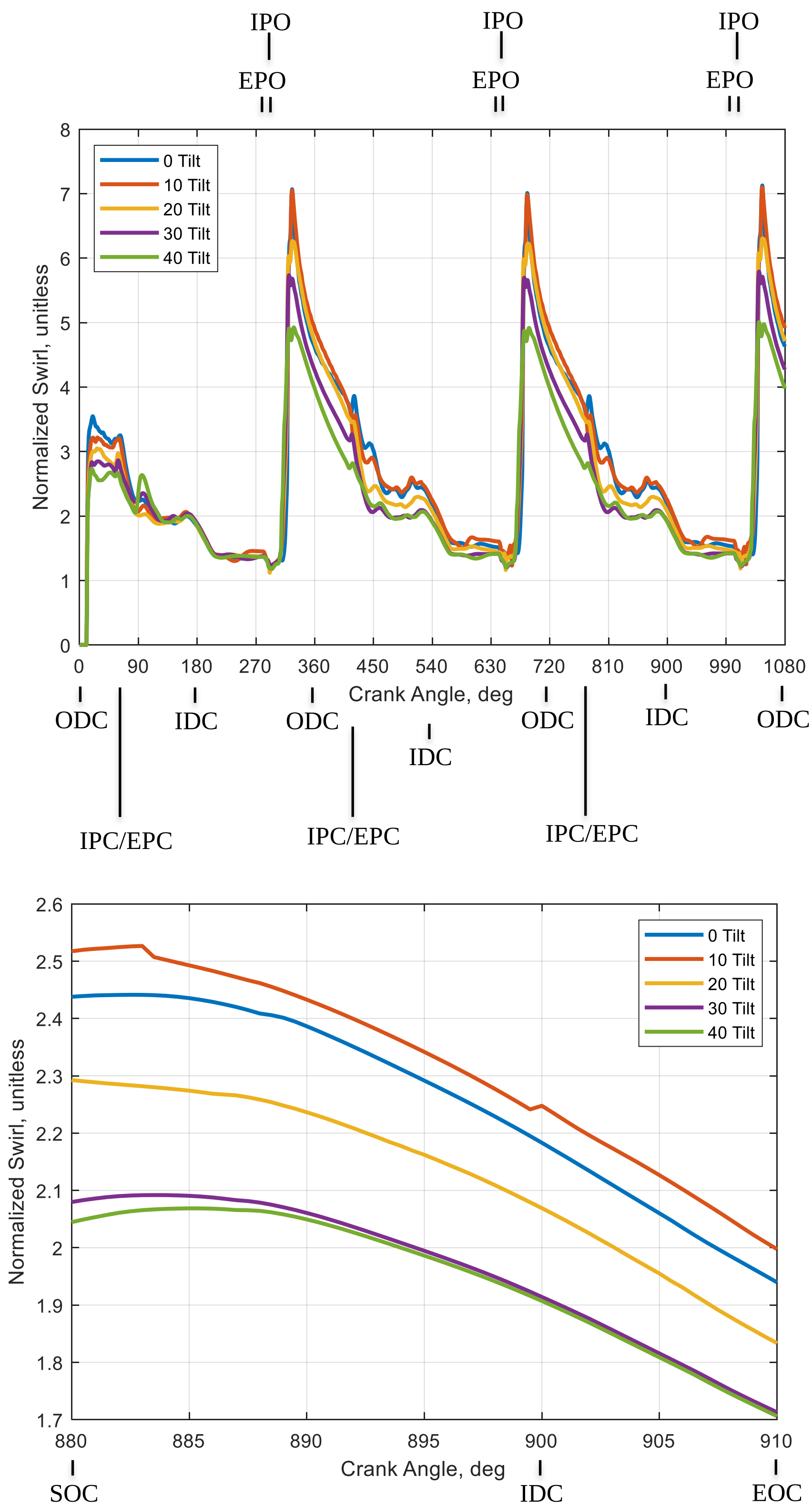

Figure 4.4. Example of flow parameter plot used throughout parameter sweep comparisons. This flow parameter plot illustrates the port timing, piston timing, and combustion timing events.

4.3.1. Tilt Angle

The first parameter sweep considered test cases with varying tilt angle. A subset of Table 3.1, shown in Table 4.4, lists the test case parameters for each tilt angle.

Table.4.4. Tilt angle parameter sweep.

Tilt Angle Sweep			
Test Case	Swirl Angle, deg	Tilt Angle, deg	Lead Angle, deg
1	15	0	10
2	15	10	10
3	15	20	10
4	15	30	10
5	15	40	10

In the following sections, engine efficiencies and transient flow parameters were investigated to observe the overall cycle behavior (engine efficiencies) and the flow behavior within each cycle as the tilt angle was changed.

4.3.1.1. Trapping Efficiency, Scavenging Efficiency, and Delivery Ratio

The effect of tilt angle on the engine's efficiencies was important when optimizing the transfer port's tilt angle. First, the scavenging efficiency was evaluated, as shown in Figure 4.5. Tilt angle's effect on scavenging efficiency was negligible with a range of only 0.14% for all tilt angle test cases.

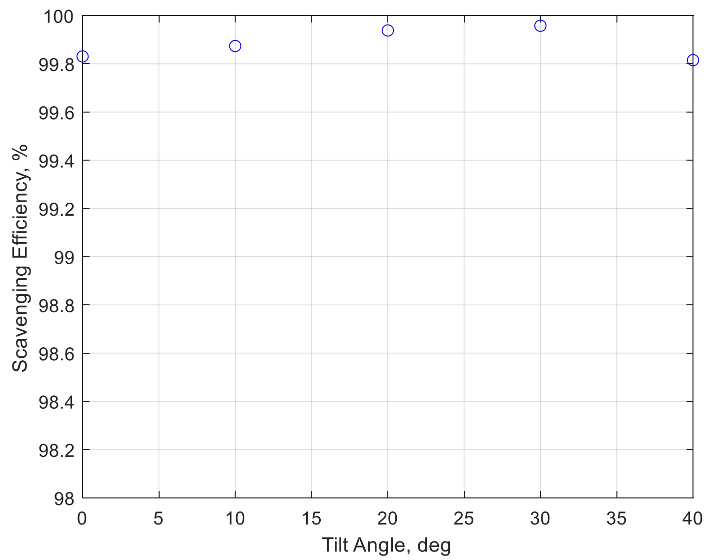

Figure 4.5. Scavenging efficiency of each test case for varying transfer port tilt angle.

Next, the trapping efficiency of the engine was investigated. Figure 4.6 displays the trend of trapping efficiency as tilt angle was increased. Observing the negatively sloped linear pattern revealed an inverse relationship between trapping efficiency and tilt angle. But, the trapping efficiency exhibited a range of only 0.98%. At 0 degrees tilt angle, trapping efficiency was 23.5%, while at 40 degrees tilt angle, trapping efficiency decreased to 22.5%.

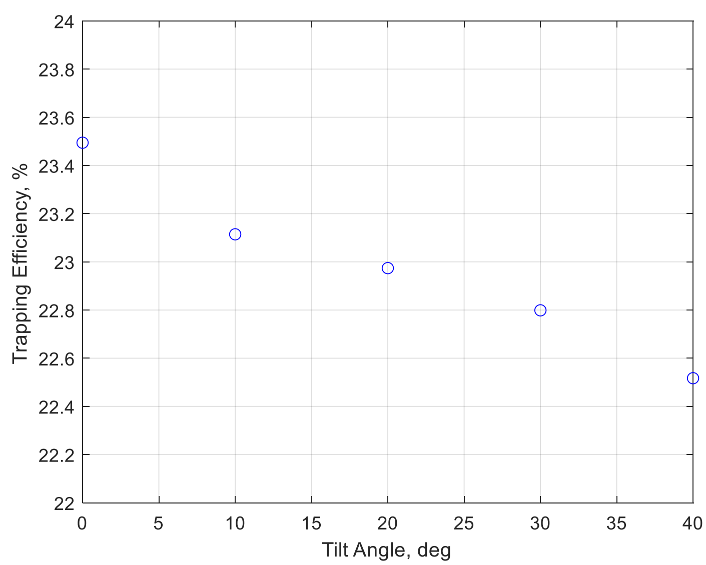

Figure 4.6. Trapping efficiency of each test case for varying transfer port tilt angle.

Finally, the delivery ratio of the engine is observed in Figure 4.7 for each tilt case. The delivery ratio exhibited a direct relationship with tilt angle. As tilt angle was increased from 0 to 40 degrees, delivery ratio increased from 5.73 to 6.02. The increase in delivery ratio equated to a 5.06% change due to tilt angle. After evaluating the overall cycle behavior with scavenging efficiency, trapping efficiency, and delivery ratio, the intracycle behavior was assessed using normalized circulation and normalized TKE.

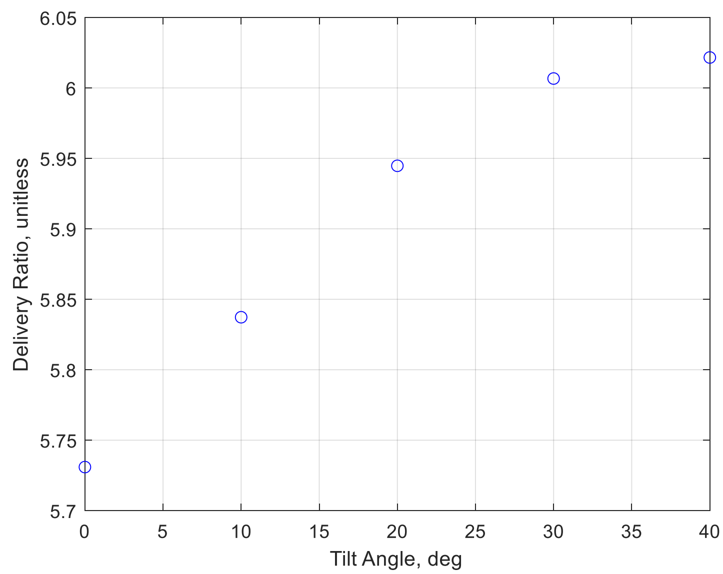

Figure 4.7. Delivery ratio of each test case for varying transfer port tilt angle.

4.3.1.2. TKE, Swirl, and Tumble

First, the relationship between crank angle and normalized turbulent kinetic energy (TKE) was evaluated, as seen in Figure 4.8. The upper plot contains information from the entire transient simulation, while the lower plot focuses on the crank angles when the combustion simulation occured. Observing the combustion crank angles was important because turbulence aids in fuel-air mixing and flame propagation (Turns, 2012).

In the upper plot for the tilt angle test cases, peak normalized turbulent kinetic energy values ranged from 194.6 for 20 degrees tilt to 219.4 for 0 degrees tilt. These peak values occurred after the intake ports opened at 680 degrees crank angle. Then, as the pistons moved to inner dead center (IDC) and the ports began closing, normalized TKE decreased until a small local maximum caused by the exhaust port closing (EPC). When the exhaust port closed at 778 degrees crank angle, normalized TKE ranged from 32.19 at 20 degrees tilt to 42.83 at 40 degrees tilt.

In the lower plot, once combustion started at 880 degrees crank angle, normalized TKE was further reduced to a range of 0.71 for 40 degrees tilt angle to 1.27 for 0 degrees tilt.

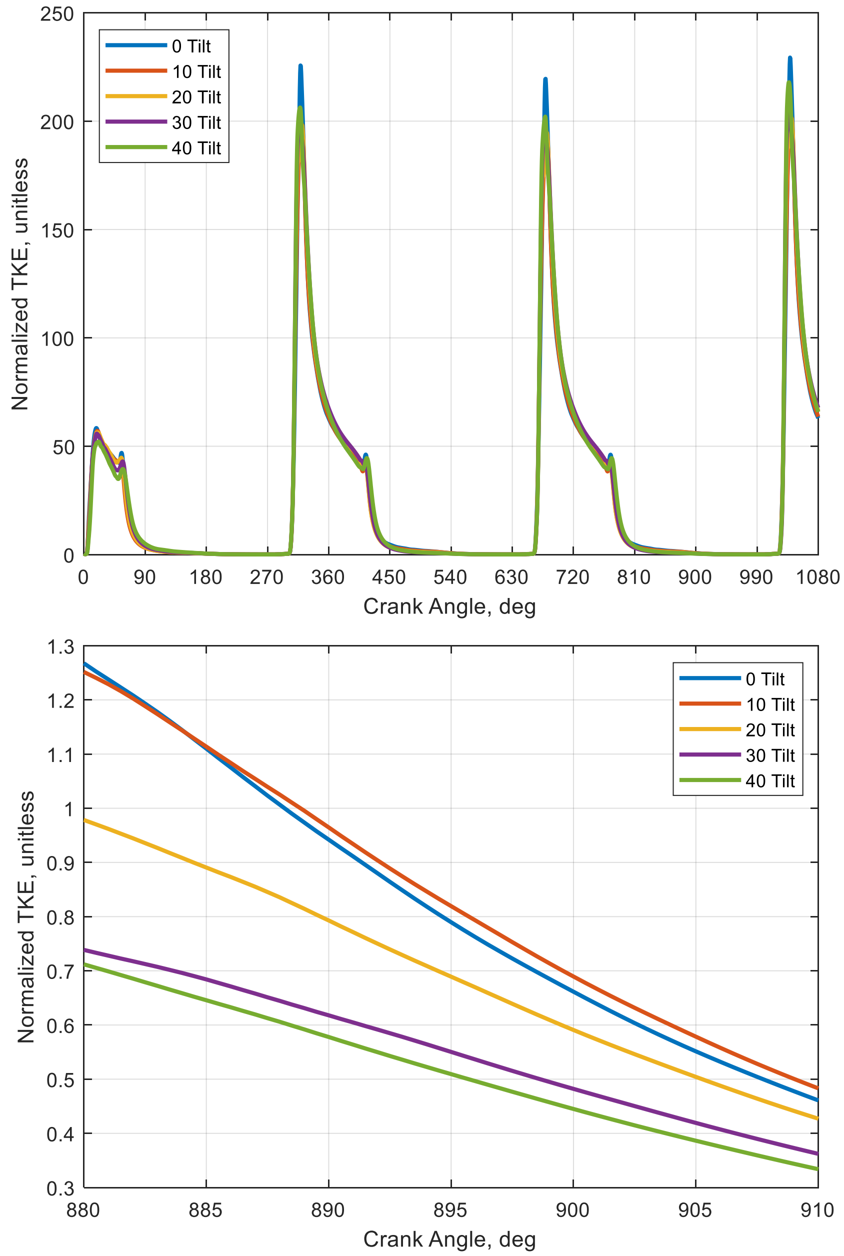

Figure 4.8. Transient, normalized TKE data of each test case for varying transfer port tilt angle. The top plot includes the full transient simulation performed in ANSYS Fluent while the bottom plot is constrained to values during the combustion simulation.

Next, Figure 4.9 depicts the relationship between crank angle and normalized swirl circulation. The upper plot contains information from the entire transient simulation. The lower plot focuses on the crank angles when the combustion simulation was taking place. Considering the crank angles where combustion takes place is important because swirl circulation aids in fuel-air mixing (Changlu et al., 2015).

In the upper plot for the tilt angle test cases, peak normalized swirl circulation ranged from 4.92 for 40 degrees tilt to 6.99 for 10 degrees tilt. These peak values occurred after the intake ports opened at 685 degrees crank angle. Then, as the pistons moved to IDC and the ports closed, normalized swirl circulation decreased until a small local maximum, where combustion began, at 880 degrees. In the lower plot, at 880 degrees, normalized swirl circulation ranged from 2.05 at 40 degrees tilt to 2.52 at 10 degrees tilt.

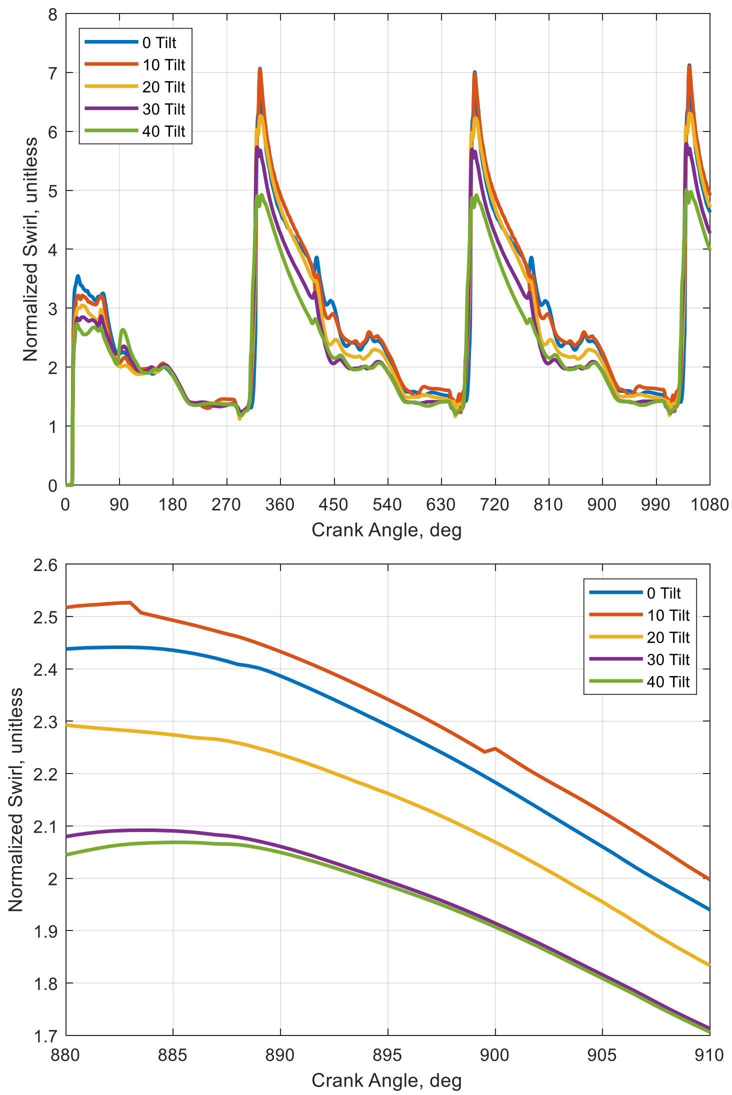

Figure 4.9. Transient, normalized swirl circulation of each test case for varying transfer port tilt angle. The top plot includes the full transient simulation performed in ANSYS Fluent while the bottom plot is constrained to values during the combustion simulation.

The behavior of normalized tumble circulation concerning increasing transfer port tilt angle was surprising for the tilt test cases. As the tilt angle of the transfer port was increased, the normalized tumble circulation decreased. As seen in Figure 4.10, the y-velocities for 0 degrees tilt angle and 40 degrees tilt angle were investigated to determine the cause of the decrease in normalized tumble circulation. Then, the x-vorticities were compared in Figure 4.11. The resulting integral of x-vorticity, or tumble circulation, of each test case, produced the inverse relationship between tumble and tilt angle.

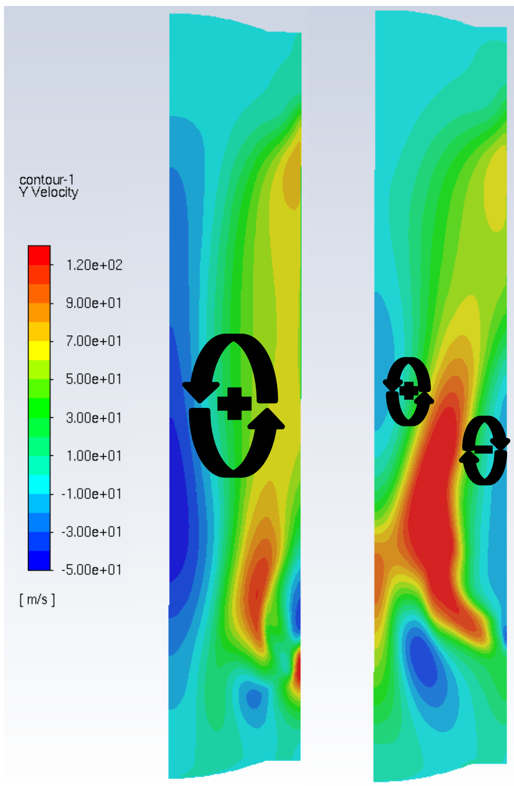

Figure 4.10. Comparison of y-velocity for 0 degrees tilt angle (left) and 40 degrees tilt angle (right). Vorticity values are represented by the black arrows on each contour plot.

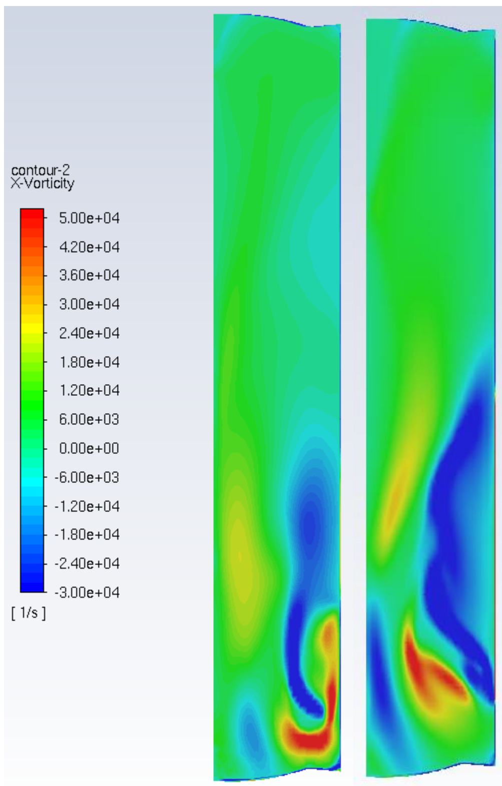

Figure 4.11. X-vorticity contours for 0 degrees tilt angle (left) and 40 degrees tilt angle (right).

Figure 4.12 presents the relationship between crank angle and normalized tumble circulation. The upper plot contains information from the entire transient simulation, while the lower plot focuses on the crank angles when the combustion simulation was taking place. The comparison plot for normalized tumble circulation was different than the normalized TKE or normalized swirl circulation cases. Due to the oscillatory nature of tumble when the ports were closed, the simulation data and the trend of the data's amplitude are presented. The trend lines allow for an easier comparison of the tumble's intensity during the combustion simulation.

In the upper plot for the tilt angle test cases, peak normalized tumble circulation ranged from 5.78 for 40 degrees tilt to 65.1 for 10 degrees tilt. These peak values occurred after the intake ports opened at 680 degrees crank angle. Then, as the pistons moved to IDC and the ports began closing, normalized tumble circulation decreased and became oscillatory once the exhaust port was closed. When the exhaust port closed at 778 degrees crank angle, normalized tumble circulation ranged from 5.31 at 40 degrees tilt to 18.9 at 10 degrees tilt.

In the lower plot, once combustion started at 880 degrees crank angle, normalized tumble circulation oscillated for all cases. But, the same trend existed (as displayed by the dashed lines) with 40 degrees tilt maintaining the lowest normalized tumble circulation and 10 degrees tilt maintaining the highest.

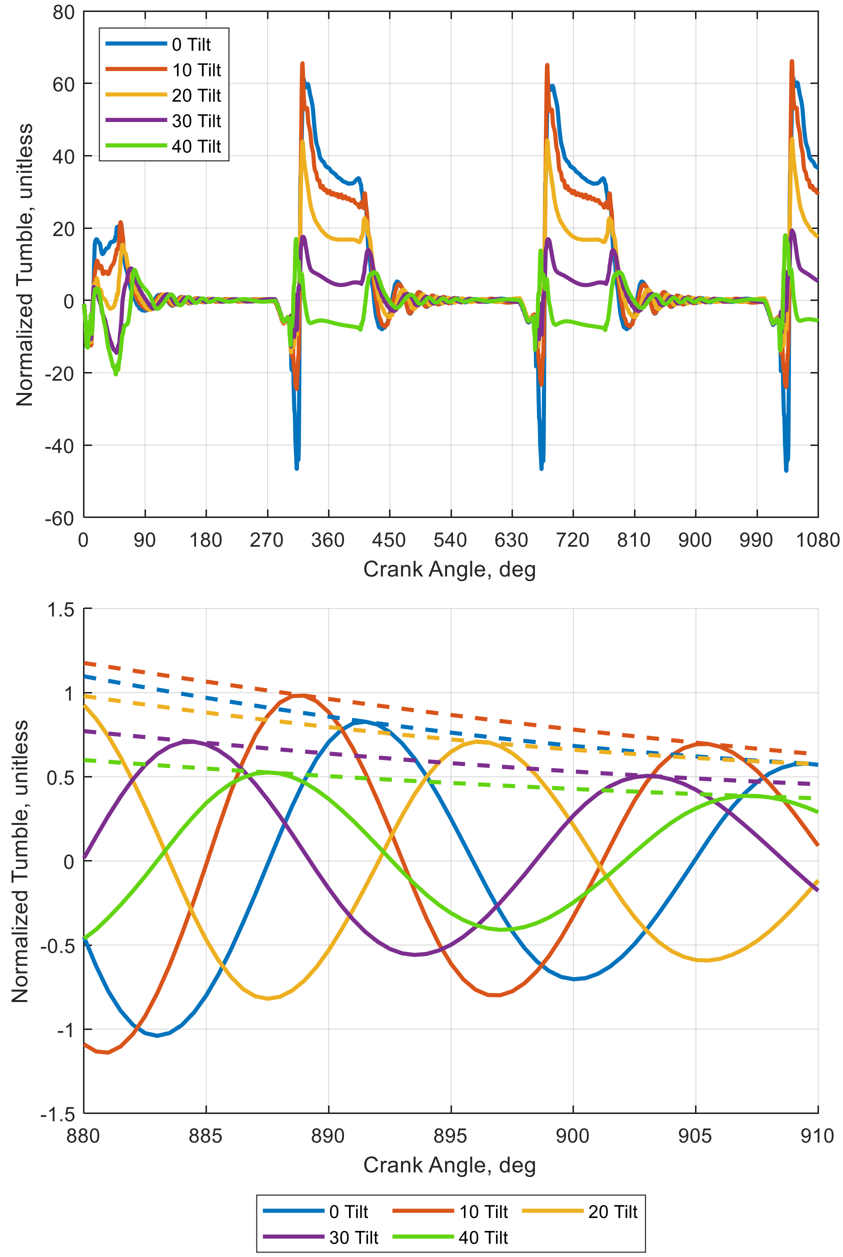

Figure 4.12. Transient, normalized tumble circulation of each test case for varying transfer port tilt angle. The top plot includes the full transient simulation performed in ANSYS Fluent, while the bottom plot is constrained to values during the combustion simulation.

4.3.2. Swirl Angle

The second parameter sweep considered test cases with varying swirl angle. A subset of Table 3.1 shown in Table 4.5**Error! Reference source not found.**, lists the test case parameters for each swirl angle.

Table 4.5. Swirl angle parameter sweep.

Swirl Angle Sweep			
Test Case	Swirl Angle, deg	Tilt Angle, deg	Lead Angle, deg
6	0	15	10
7	7.5	15	10
8	15	15	10
9	22.5	15	10
10	30	15	10

In the following sections, engine efficiencies, as well as transient flow parameters, are investigated to observe the overall cycle behavior as well as the flow behavior within each cycle as swirl angle was changed.

4.3.2.1. Trapping Efficiency, Scavenging Efficiency, and Delivery Ratio

The effect of swirl angle on the engine's efficiencies is important to consider when optimizing the transfer port's geometry. First, the scavenging efficiency was evaluated, as shown in Figure 4.13. Swirl angle impacted scavenging efficiency more than tilt angle or exhaust piston lead angle, but the range was still only 0.7%. Therefore, the effect of swirl angle on scavenging efficiency was considered negligible.

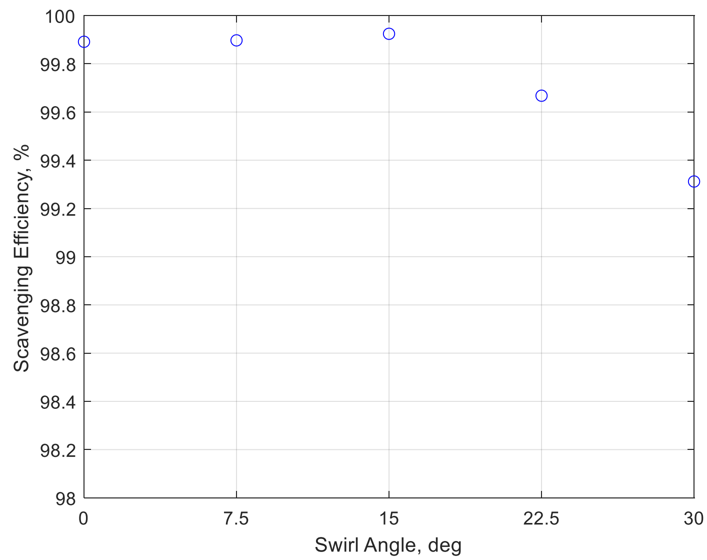

Figure 4.13. Scavenging efficiency of each test case for varying transfer port swirl angle.

Next, the trapping efficiency of the engine was investigated. Figure 4.14 displays the trend of trapping efficiency as swirl angle was increased. The trapping efficiency exhibited an odd relationship with swirl angle. At 7.5 degrees swirl angle, there was a comparatively large drop in trapping efficiency, but the range of trapping efficiencies was only 0.3%. Therefore, the effect of swirl angle on trapping efficiency was also negligible.

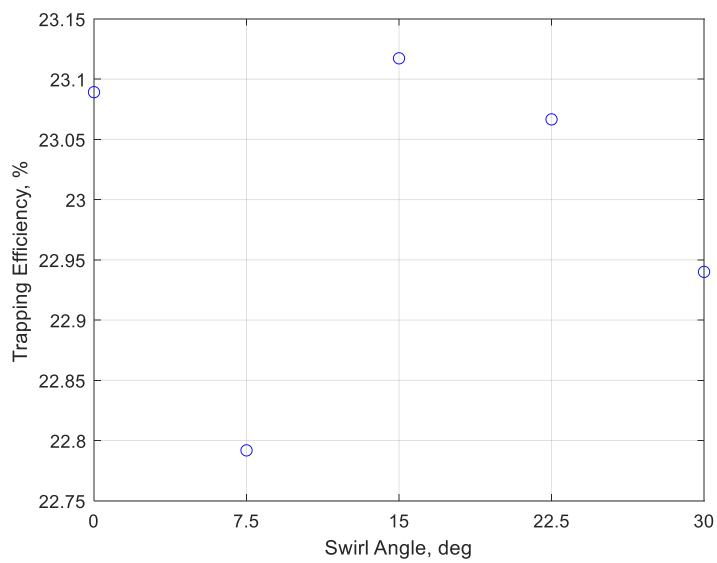

Figure 4.14. Trapping efficiency of each test case for varying transfer port swirl angle.

Figure 4.15 describes the delivery ratio of the engine cycle for each swirl case. The delivery ratio exhibited a peak value at 7.5 degrees swirl angle. As swirl angle was increased or decreased from this point, delivery ratio also decreased. Physically, this represented that the largest amount of fresh air was delivered through the intake port at 7.5 degrees of swirl angle. The peak delivery ratio experienced at 7.5 degrees swirl angle was 6.03, while the lowest delivery ratio observed at 30 degrees swirl angle was 5.70. Therefore, altering the swirl angle produced up to a 5.79% increase in delivery ratio.

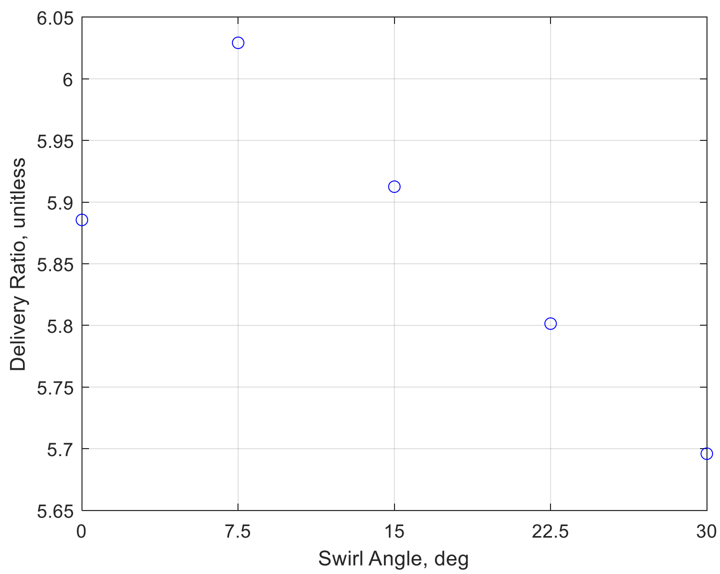

Figure 4.15. Delivery ratio of each test case for varying transfer port swirl angle.

4.3.2.2. TKE, Swirl, and Tumble

After investigating the overall cycle behavior for changes in swirl angle, the intracycle behavior was observed. Figure 4.16 illustrates the relationship between crank angle and normalized turbulent kinetic energy (TKE). The upper plot contains information from the entire transient simulation. The lower plot focuses on the crank angles when the combustion simulation was taking place.

In the upper plot for the swirl angle test cases, peak normalized turbulent kinetic energy ranged from 144.0 for 40 degrees swirl to 201.3 for 15 degrees swirl. These peak values occurred after the intake ports opened at 680 degrees crank angle. Then, as the pistons moved to inner dead center (IDC) and the ports began closing, normalized TKE decreased until a small local maximum at exhaust port closing (EPC) occured. When the exhaust port closed at 778 degrees crank angle, normalized TKE ranged from 22.69 at 40 degrees swirl to 32.96 at 7.5 degrees tilt.

In the lower plot, once combustion started at 880 degrees crank angle, normalized TKE was further reduced to a range of 0.56 for 0 degrees tilt angle to 2.00 for 40 degrees tilt angle. Comparing the upper and lower plots shows the swirl cases produced opposite trends between ports open and ports closed. As swirl angle increased, peak normalized TKE values decreased during ports open. During ports closed, the trend reversed with increasing swirl angle resulting in increasing normalized TKE.

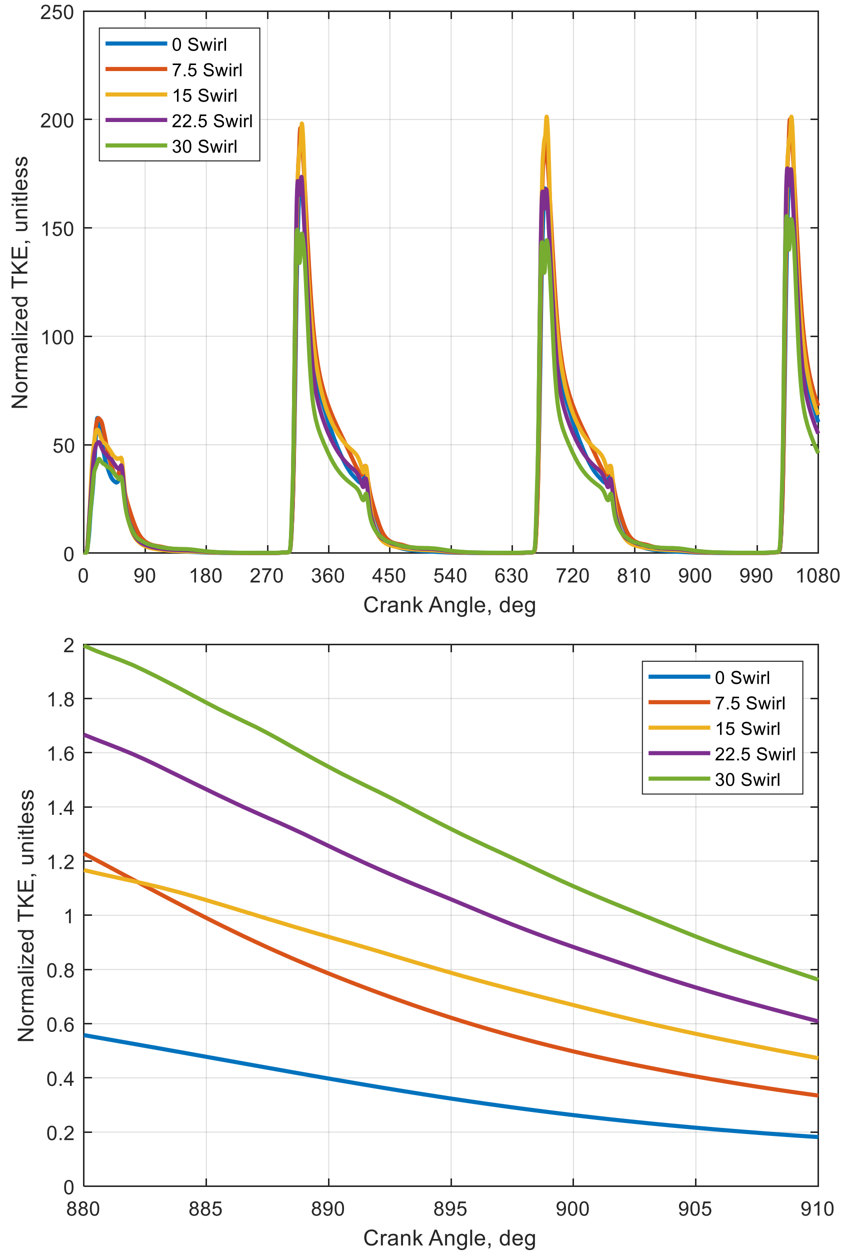

Figure 4.16. Transient, normalized TKE data of each test case for varying transfer port swirl angle. The top plot includes the full transient simulation performed in ANSYS Fluent while the bottom plot is constrained to values during the combustion simulation.

Figure 4.17 depicts the relationship between crank angle and normalized swirl circulation. The upper plot contains information from the entire transient simulation. The lower plot focuses on the crank angles when the combustion simulation was taking place. The normalized swirl circulation was compared while the ports were open and while the ports were closed.

In the upper plot for the swirl angle test cases, peak normalized swirl circulation ranged from 0.09 for 0 degrees swirl to 9.42 for 30 degrees swirl. These peak values occurred after the intake ports opened at 685 degrees crank angle. Then, as the pistons moved to IDC and the ports closed, normalized swirl circulation decreased until a small local maximum, where combustion began, at 880 degrees. In the lower plot, at 880 degrees, normalized swirl circulation ranged from 0.01 at 0 degrees swirl to 3.66 at 30 degrees swirl.

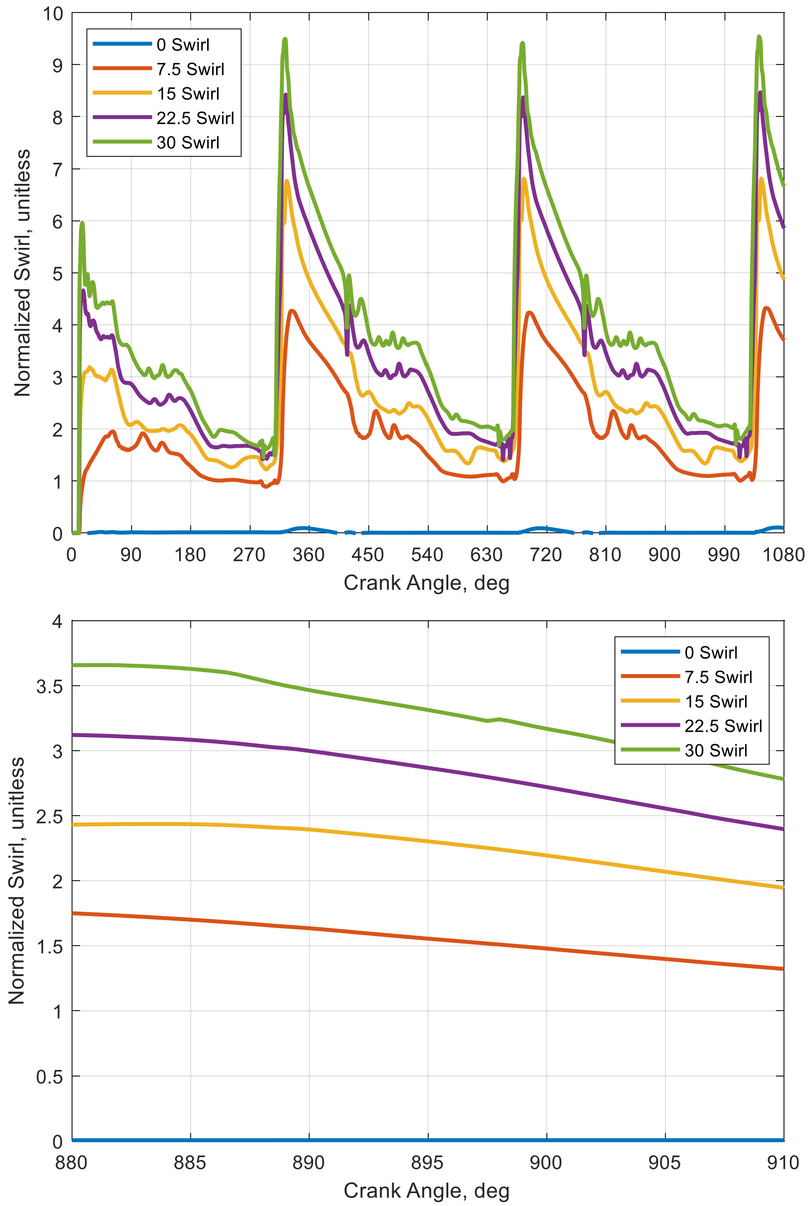

Figure 4.17. Transient, normalized swirl circulation of each test case for varying transfer port swirl angle. The top plot includes the full transient simulation performed in ANSYS Fluent while the bottom plot is constrained to values during the combustion simulation.

An interesting trend emerged for normalized tumble circulation as the swirl angle of the transfer port was changed. At 0 degrees and 7.5 degrees swirl angle, the normalized tumble circulation was negative, but for all other swirl angles, the normalized tumble circulation was positive. To verify this surprising behavior was not caused by miscalculations, contours of y-velocity were compared since it is the dominant velocity within the cylinder. Figure 4.18 illustrates the cause of the switch in sign for normalized tumble circulation. At lower swirl angles, the upward-flowing air is pushed to the middle of the cylinder, while at higher swirl angles, the upward-flowing air is pushed to the outside of the cylinder.

Then, the resulting contours of x-vorticity are depicted in Figure 4.19, which were integrated to generate tumble circulation. As expected, the test case with 0 degrees swirl angle exhibited negative x-vorticity, while the test case with 30 degrees swirl angle produced positive x-vorticity.

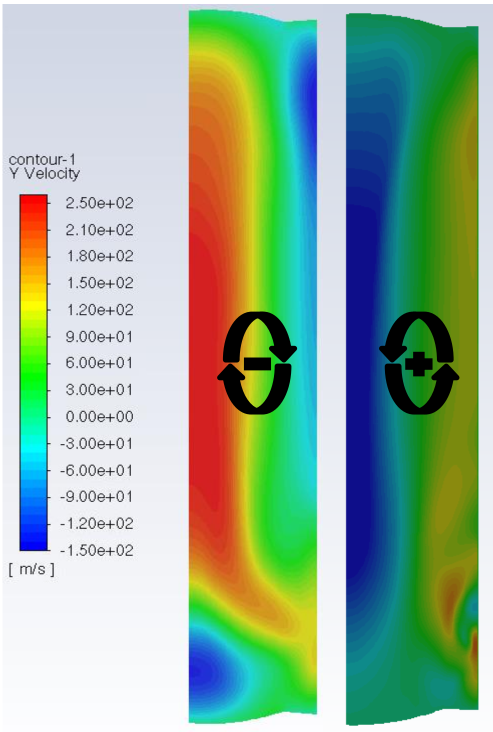

Figure 4.18. Comparison of y-velocity for 0 degrees swirl angle (left) and 30 degrees swirl angle (right). Vorticity values are represented by the black arrows on each contour plot and shown in Figure 4.19.

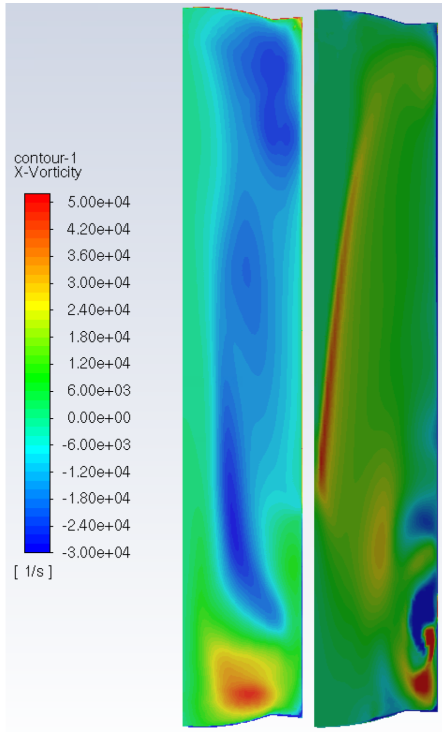

Figure 4.19. X-vorticity contours for 0 degrees swirl angle (left) and 30 degrees swirl angle (right).

Figure 4.20 presents the relationship between crank angle and normalized tumble circulation. The upper plot contains information from the entire transient simulation. In contrast, the lower plot focuses on the crank angles when the combustion simulation was taking place. The comparison plot for normalized tumble circulation was different than the normalized TKE or normalized swirl circulation cases. Due to the oscillatory nature of tumble, the actual data is presented along with the trend of the data's amplitude when the ports were closed. The trend lines allow for an easier comparison of the tumble's intensity during the combustion simulation.

In the upper plot for the swirl angle test cases, peak normalized tumble circulation ranged from -100.7 for 0 degrees swirl to 105.9 for 30 degrees swirl. These peak values occurred after the intake ports opened at 680 degrees crank angle. Then, as the pistons moved to IDC and the ports began closing, normalized tumble circulation decreased and became oscillatory once the exhaust port was closed. When the exhaust port closed at 778 degrees crank angle, normalized tumble circulation ranged from -28.52 at 0 degrees swirl to 21.11 at 15 degrees swirl.

In the lower plot, once combustion started at 880 degrees crank angle, normalized tumble circulation was oscillatory for all cases. But, the same trend existed (as displayed by the dashed lines) with 0 degrees swirl maintaining the lowest normalized tumble circulation and 30 degrees swirl maintaining the highest normalized tumble circulation.

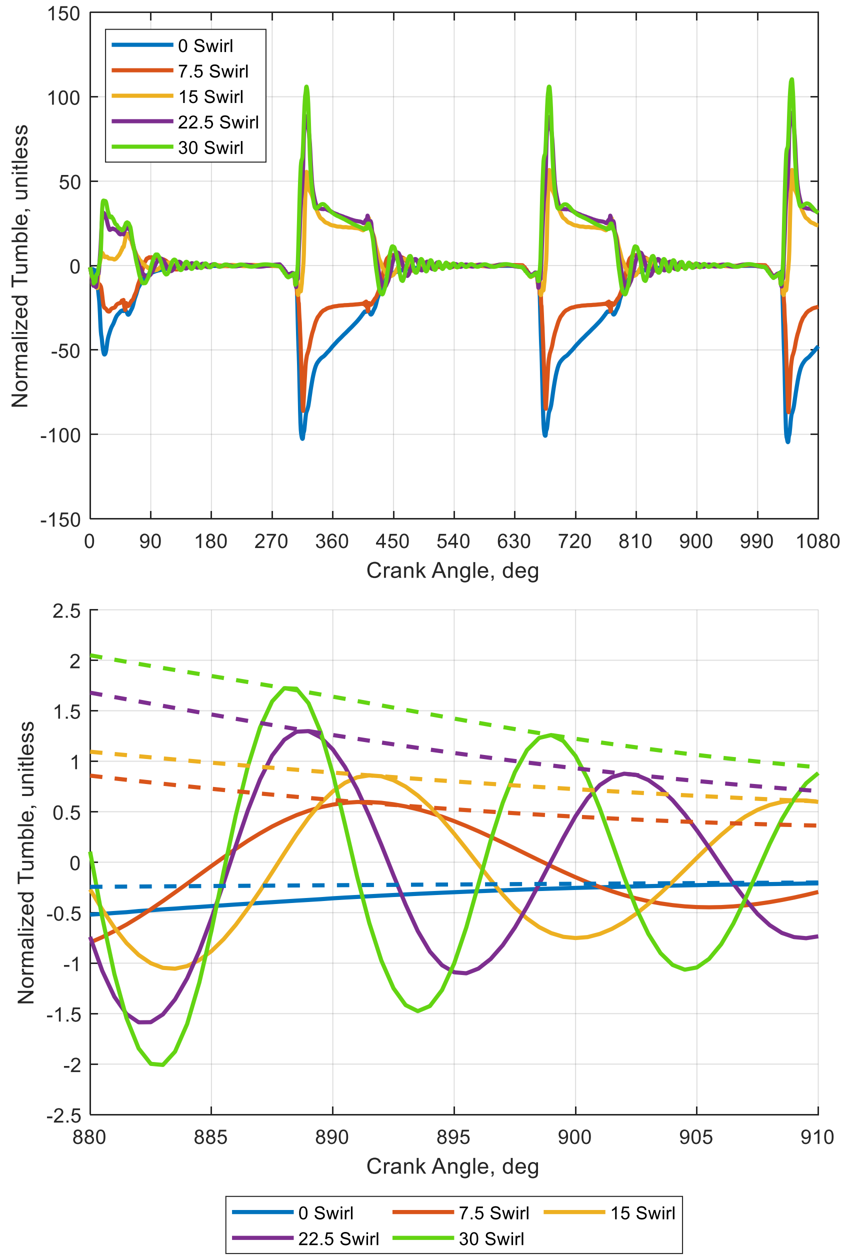

Figure 4.20. Transient, normalized tumble circulation of each test case for varying transfer port swirl angle. The top plot includes the full transient simulation performed in ANSYS Fluent while the bottom plot is constrained to values during the combustion simulation.

4.3.3. Exhaust Piston Lead Angle

The third parameter sweep considered test cases with varying exhaust piston lead angle. Table 3.2 , lists the test case parameters for each exhaust piston lead angle.

In the following sections, engine efficiencies, as well as transient flow parameters, are investigated to observe the overall cycle behavior, as well as the flow behavior within each cycle as exhaust piston lead angle was changed.

4.3.3.1. Trapping Efficiency, Scavenging Efficiency, and Delivery Ratio

First, the effect of exhaust piston lead angle on the engine's efficiencies was considered when optimizing the port timing of the engine. Figure 4.21 illustrates the change in scavenging efficiency as exhaust piston lead angle was changed. Like transfer port geometry, exhaust piston lead angle caused a negligible change in scavenging efficiency. Through each exhaust piston lead angle test case, the scavenging efficiency only changed 0.19%.

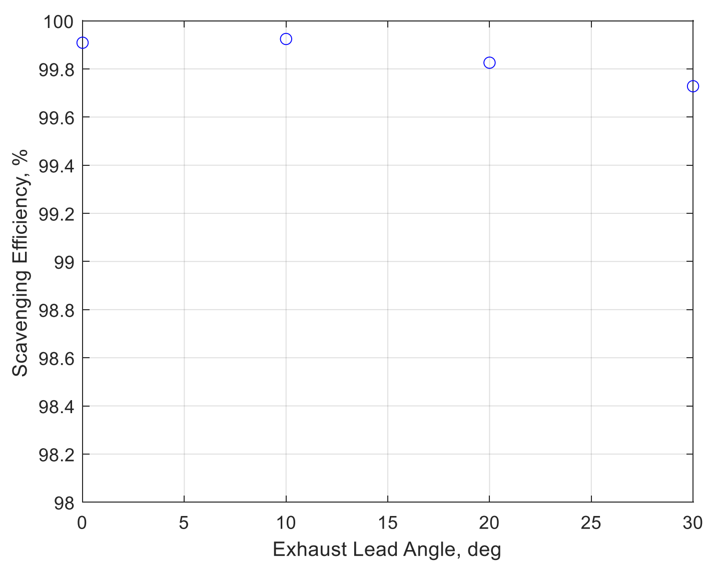

Figure 4.21. Scavenging efficiency of each test case for varying exhaust piston lead angle.

Next, the trapping efficiency of the engine was investigated. Figure 4.22 displays the trend of trapping efficiency as exhaust piston lead angle was increased. For exhaust piston lead angle, the trapping efficiency was optimized at 20 degrees. There was a sharp decline in trapping efficiency for smaller lead angles, while the trapping efficiency was similar for 20 and 30 degrees. Exhaust piston lead angle changed trapping efficiency from 17.7% with 0 degrees exhaust piston lead angle to 26.1% with 20 degrees exhaust piston lead angle.

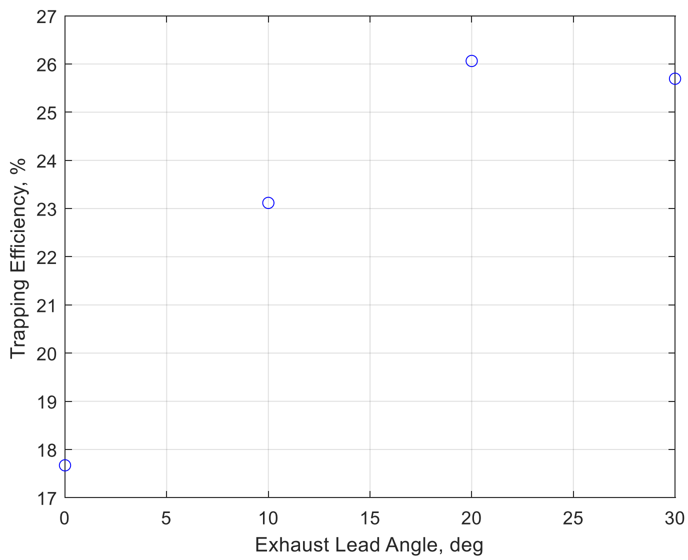

Figure 4.22. Trapping efficiency of each test case for varying exhaust piston lead angle.

Finally, Figure 4.23 describes the delivery ratio of the engine cycle for each exhaust piston lead angle case. For exhaust piston lead angle test cases, the delivery ratio was optimized at a lead angle of 10 degrees. At 30 degrees exhaust piston lead angle, the delivery ratio was 5.20, while at 10 degrees exhaust piston lead angle, the delivery ratio was 5.91. Physically, this represented a 13.7% increase in the amount of fresh charge delivered through the intake port.

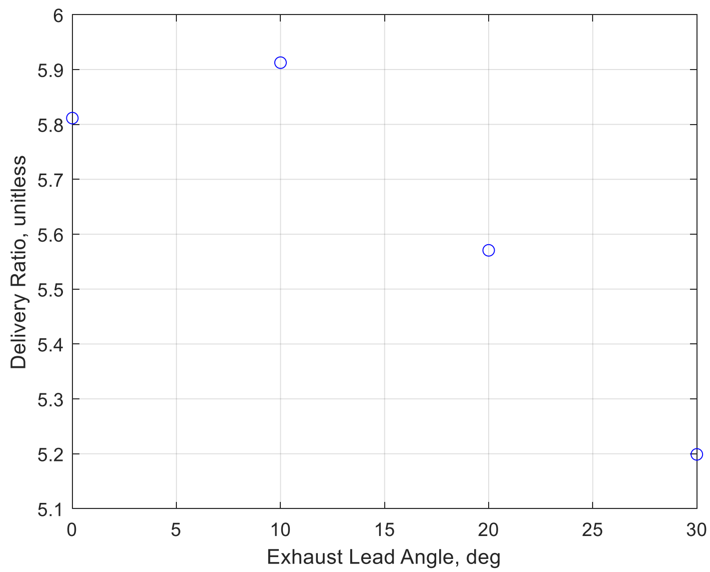

Figure 4.23. Delivery ratio of each test case for varying exhaust piston lead angle.

4.3.3.2. TKE, Swirl, and Tumble

After investigating engine efficiencies, the transient flow parameters were considered, which described intracycle behavior. Figure 4.24 illustrates the relationship between crank angle and normalized turbulent kinetic energy (TKE). The upper plot contains information from the entire transient simulation, while the lower plot focuses on the crank angles when the combustion simulation was taking place. For exhaust piston lead, test cases with lower lead angles presented higher normalized TKE values during the air charge exchange and combustion processes.

In the upper plot for the exhaust piston lead angle test cases, peak normalized turbulent kinetic energy ranged from 161.1 for 30 degrees exhaust piston lead angle to 201.3 for 10 degrees exhaust piston lead angle. These peak values occurred after the intake ports opened at 680 degrees crank angle. Then, as the pistons approached IDC and the ports began closing, normalized TKE decreased until a small local maximum at exhaust port closing (EPC) occurred. When the exhaust port closed, normalized TKE ranged from 14.20 at 0 degrees lead angle to 33.68 at 30 degrees lead. In the lower plot, once combustion started at 880 degrees crank angle, normalized TKE was further reduced to 0.90 for 30 degrees lead angle and 1.17 for 10 degrees lead angle.

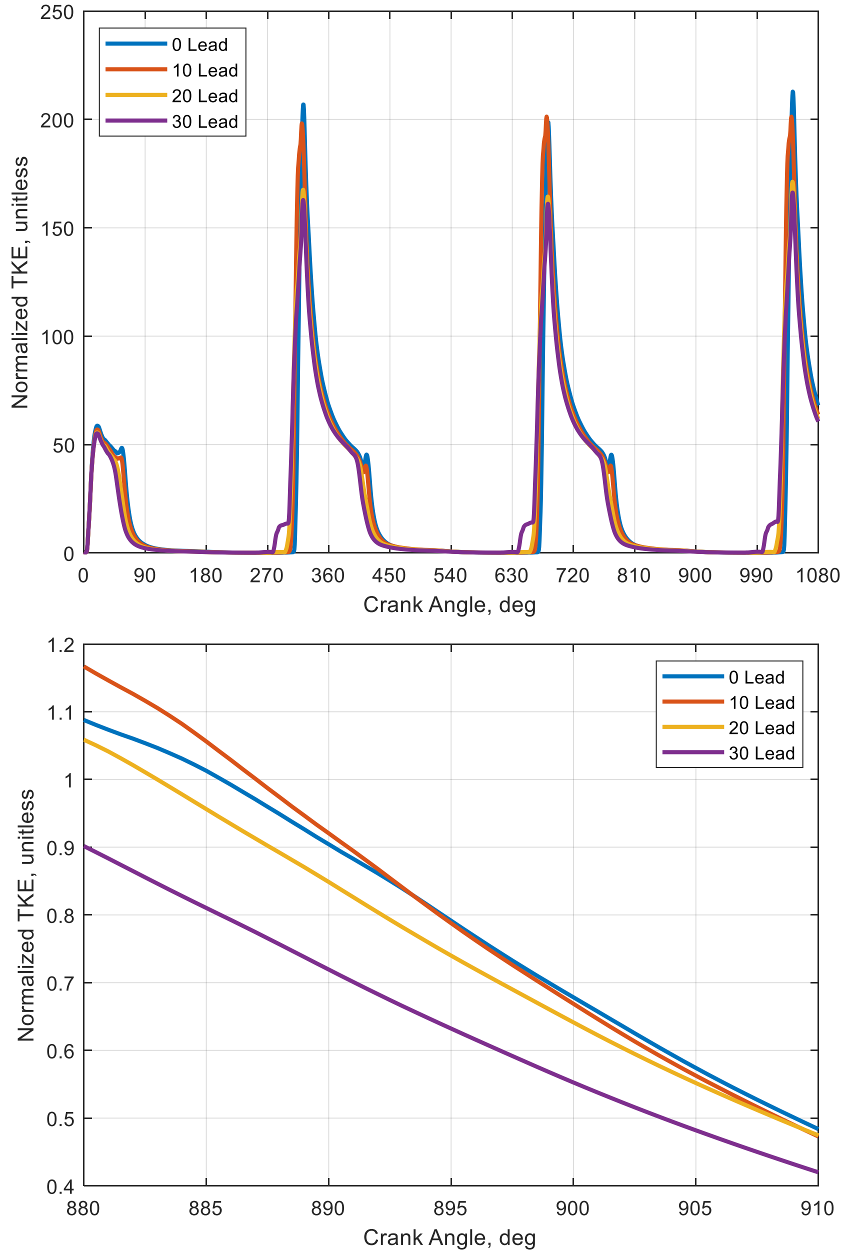

Figure 4.24. Transient, normalized TKE data of each test case for varying exhaust piston lead angle. The top plot includes the full transient simulation performed in ANSYS Fluent while the bottom plot is constrained to values during the combustion simulation.

Figure 4.25 depicts the relationship between crank angle and normalized swirl circulation. The upper plot contains information from the entire transient simulation. The lower plot focuses on the crank angles when the combustion simulation was taking place. The normalized swirl circulation was compared while the ports were open and while the ports were closed. With open and closed ports, 10 degrees exhaust piston lead angle produced the highest normalized swirl circulation.

In the upper plot for the exhaust piston lead angle test cases, peak normalized swirl circulation ranged rfrom 6.22 for 30 degrees exhaust piston lead angle to 6.81 for 10 degrees exhaust piston lead angle. These peak values occurred after the intake ports opened at 685 degrees crank angle. Then, as the pistons moved to IDC and the ports closed, normalized swirl circulation decreased until a small local maximum, where combustion began, at 880 degrees. In the lower plot, at 880 degrees, normalized swirl circulation ranged from 2.20 at 0 degrees lead angle to 2.43 at 10 degrees lead angle.

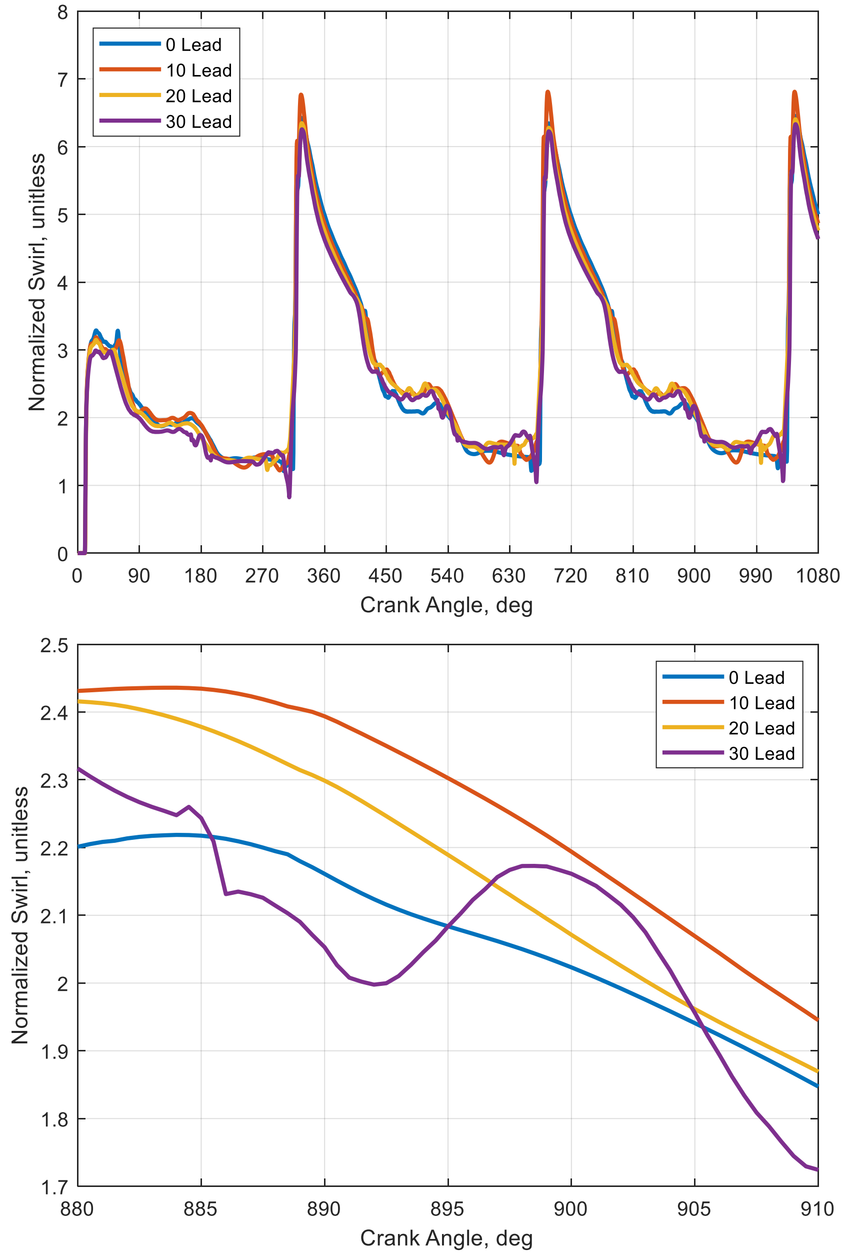

Figure 4.25. Transient, normalized swirl circulation of each test case for varying exhaust piston lead angle. The top plot includes the full transient simulation performed in ANSYS Fluent while the bottom plot is constrained to values during the combustion simulation.

Figure 4.26 presents the relationship between crank angle and normalized tumble circulation. The upper plot contains information from the entire transient simulation. The lower plot focuses on the crank angles when the combustion simulation was taking place. The comparison plot for normalized tumble circulation was different than the normalized TKE or normalized swirl circulation cases. Due to the oscillatory nature of tumble when the ports were closed, the actual data is presented along with the trends of the data's amplitude. The trend lines allow for an easier comparison of the tumble's intensity during the combustion simulation.

In the upper plot for the exhaust piston lead angle test cases, peak normalized tumble circulation ranged from 48.6 for 30 degrees exhaust piston lead angle to 68.3 for 0 degrees exhaust piston lead angle. These peak values occurred after the intake ports opened at 680 degrees crank angle. Then, as the pistons moved to IDC and the ports began closing, normalized tumble circulation decreased and became oscillatory once the exhaust port was closed. When the exhaust port closed, normalized tumble circulation ranged from 10.8 at 0 degrees lead angle to 23.9 at 20 degrees lead angle.

In the lower plot, once combustion started at 880 degrees crank angle, normalized tumble circulation was oscillatory for all cases. When comparing the upper and lower plots, the trend in normalized tumble circulation did not remain the same between ports open and ports closed. For example, 0 degrees exhaust piston lead angle had the highest normalized tumble circulation but the lowest normalized tumble circulation amplitude during combustion.

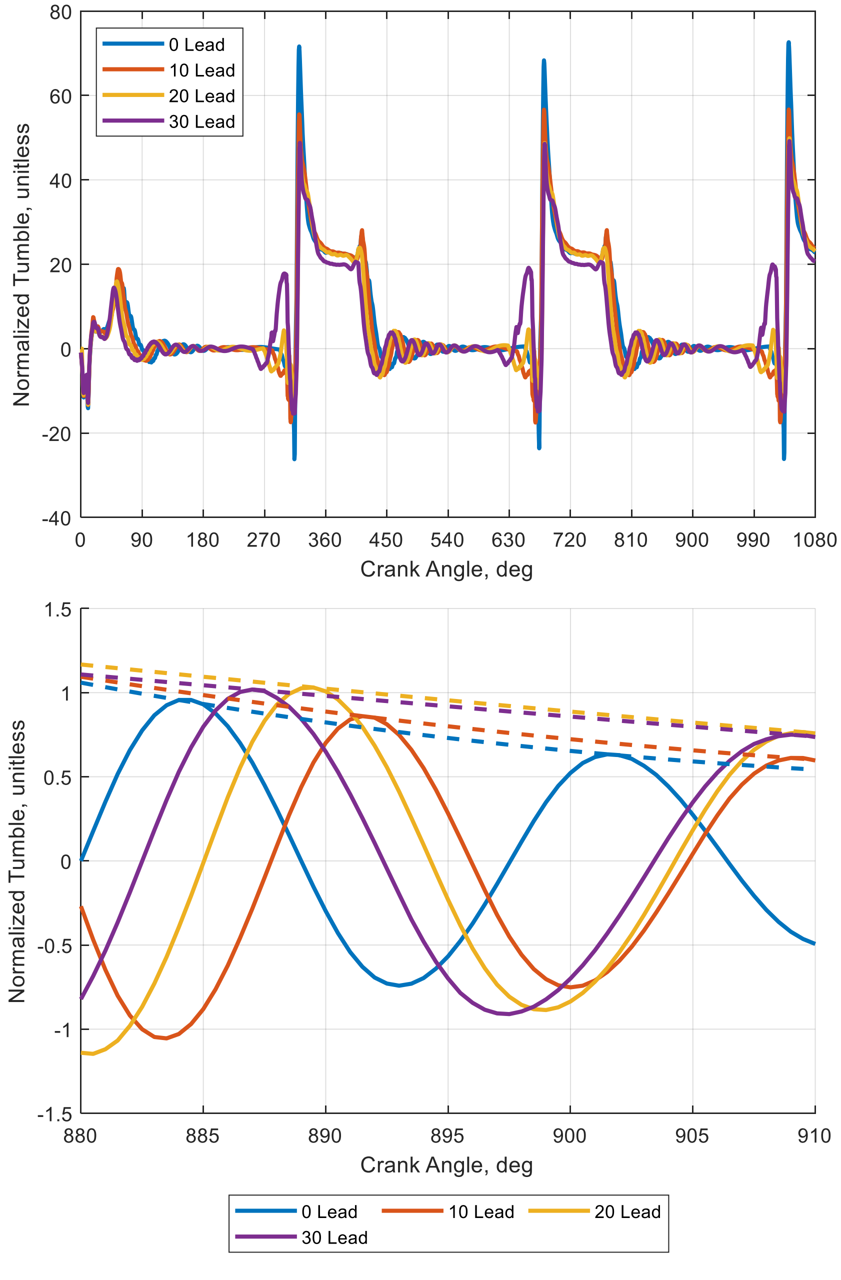

Figure 4.26. Transient, normalized tumble circulation of each test case for varying exhaust piston lead angle. The top plot includes the full transient simulation performed in ANSYS Fluent while the bottom plot is constrained to values during the combustion simulation.

4.4. OAT Sensitivity Analysis

After the values of the collected efficiencies and flow parameters were observed, the effect of each input parameter on the collected output parameters was determined. To evaluate these effects the maximum sensitivity coefficient of each output parameter was evaluated at EPC to establish whether tilt angle, swirl angle, or exhaust piston lead angle influenced the output parameters. The exhaust port closing point was selected because it is a critical point during the engine's cycle where turbulence plays a substantial role in air-fuel mixing (Changlu et al., 2015). The reactivity of each output parameter was evaluated using the maximum sensitivity coefficient. For this thesis research, sensitivity coefficients of less than 0.05 were considered negligible. This coefficient represents a change of only 0.05% in output parameter when the input parameter changes 1%. The maximum sensitivity coefficients for each output parameter are displayed in Table 4.6, along with the respective parameter sweep.

Table 4.6. Maximum sensitivity coefficients for each output parameter due to input parameter sweeps

Parameter Sweep	Scavenging Efficiency	Trapping Efficiency	Normalized Swirl Circulation	Normalized Tumble Circulation	Normalized TKE
Tilt Angle	0.0057	0.0500	0.5979	6.5288	0.7621
Swirl Angle	0.0143	0.0221	0.7435	2.0364	0.7497
Exhaust Piston Lead Angle	0.0029	0.1815	0.1091	0.5141	0.2887

As illustrated by Table 4.6, scavenging efficiency was the output parameter least affected by changes to the input parameters. For tilt angle, swirl angle, and exhaust piston lead angle, the scavenging efficiency remained above 99%, with a maximum sensitivity coefficient of 0.0143. Therefore, the effects of the input parameters on scavenging efficiency were negligible.

Trapping efficiency was not influenced by changes to the transfer port geometry but exhibited a dependence on exhaust piston lead angle. As shown in **Error! Reference source not found.**, the sensitivity coefficient for trapping efficiency was less than 0.05 for tilt angle and swirl angle, while the sensitivity coefficient was 0.18 for exhaust piston lead angle. Figure 4.27 illustrates the change in the trapping efficiency of the engine as each input parameter was changed.

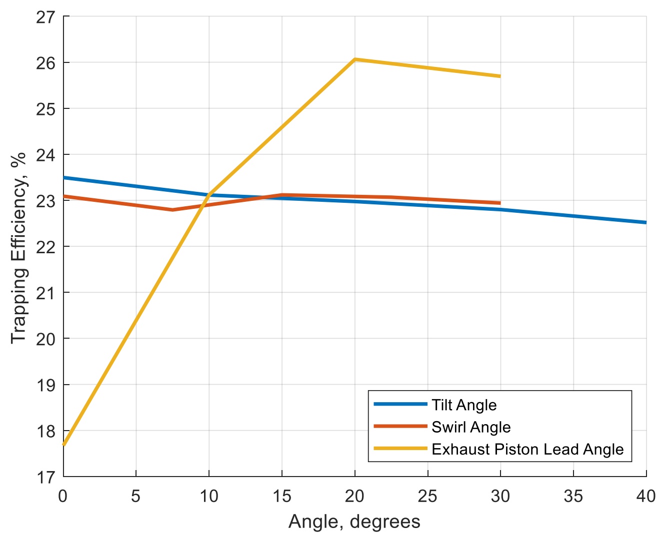

Figure 4.27. Plot of trapping efficiency with respect to input parameter angle.

Normalized swirl circulation was influenced by changes to tilt angle, swirl angle, and exhaust piston lead angle. Swirl angle had the most significant influence on normalized swirl circulation with a sensitivity coefficient of 0.74. Tilt angle followed with a coefficient of 0.60, and exhaust piston lead angle produced a coefficient of 0.11. These sensitivity coefficients showed that normalized swirl circulation was five times more sensitive to transfer port geometry than exhaust piston lead angle. Figure 4.28 displays the relationship between normalized swirl circulation and each input parameter.

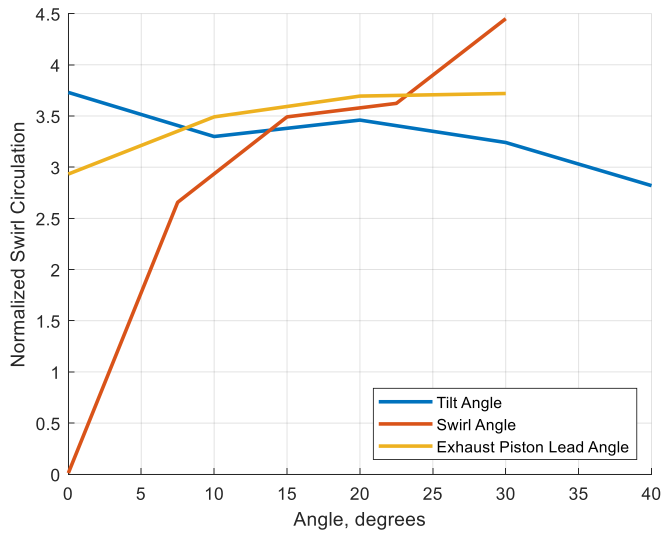

Figure 4.28. Plot of normalized swirl circulation with respect to input parameter angle.

Similar to normalized swirl circulation, normalized tumble circulation was influenced by tilt angle, swirl angle, and exhaust piston lead angle. Normalized tumble circulation experienced more significant changes with a maximum sensitivity coefficient of 6.53, compared to 0.74 for normalized swirl circulation. Changes in swirl angle generated a coefficient of 2.04, and changes in exhaust piston lead angle yielded a coefficient of 0.51. The tilt angle had a larger impact, with a sensitivity coefficient of 6.53. These high sensitivity coefficients illustrated a strong relationship between transfer port geometry and normalized tumble circulation. Also, like normalized swirl circulation, the sensitivity coefficients determined that normalized tumble circulation was four times more sensitive to changes in port geometry than changes in exhaust piston lead angle. Figure 4.29 represents the normalized tumble circulation as a function of input parameter angles. Also, as discussed in 4.3.2.2, swirl angle changes the sign of normalized tumble circulation as the parameter changes from 0 to 15 degrees.

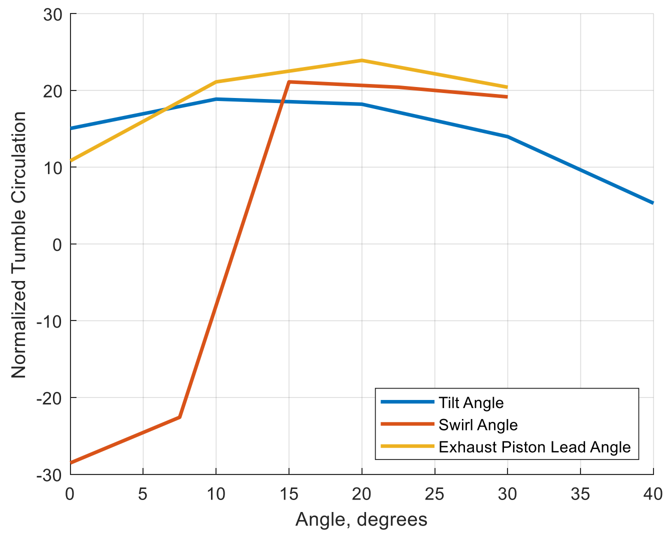

Figure 4.29. Plot of normalized tumble circulation with respect to input parameter angle.

Finally, normalized TKE was also affected by all three input parameters. The calculated sensitivity coefficients for tilt angle, swirl angle, and exhaust piston lead angle were 0.76, 0.75, and 0.29, respectively. Therefore, normalized TKE's sensitivity to the input parameters was similar to normalized swirl circulation's sensitivity. It is also important to note that normalized TKE was low at a lead angle of zero, as shown in Figure 4.30. The zero-degree lead angle data point was observed independent of the sensitivity coefficient due to the normalization process. When the sensitivity coefficient is normalized, it is multiplied by the input parameter, producing a coefficient of zero at zero exhaust piston lead angle.

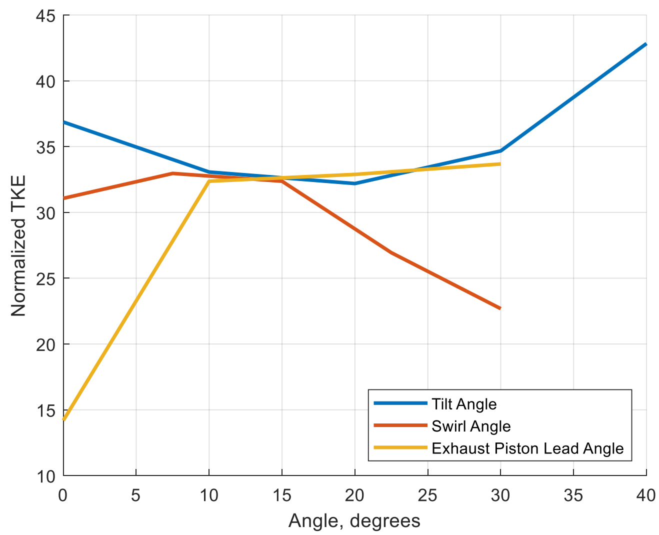

Figure 4.30. Plot of normalized TKE with respect to input parameter angle.

CHAPTER 5. SUMMARY, CONCLUSIONS, AND RECOMMENDATIONS

5.1. Summary

As the population increases, the world's energy demand also increases. According to the U.S. Energy Information Administration (EIA), since 2010, world energy consumption has risen 17% (U.S. Energy Information Administration, 2019). From today's current energy consumption of 6.5×10^{11} gigajoules, energy consumption is expected to increase an additional 46% (U.S. Energy Information Administration, 2019).

Due to the increase in power demand, CO_2 emissions and fuel consumption are expected to increase. This thesis project aims to address the emissions and fuel issues by investigating the development of a more efficient two-stroke engine to increase efficiency and reduce fuel consumption to reduce CO_2 emissions. Also, future legislation will require vehicle manufacturers to meet more stringent regulations for fleet fuel economy. In 2025, U.S. manufacturers will have to attain a fleet-wide average fuel economy of 40.6 miles per gallon (Zielinski et al., 2018).

The purpose of this project was to develop a computational fluid dynamics (CFD) model capable of simulating airflow in an opposed-piston, two-stroke engine. The model analyzed flow patterns within the engine and quantified the effect of different geometric engine parameters on engine performance.

After obtaining results from the numerical model, the engine's response to tilt angle, swirl angle, and exhaust piston lead angle was observed. As elaborated later, the exhaust piston lead angle had the largest effect on engine efficiencies. In comparison, the swirl and tilt angles produced the most significant changes for turbulence within the cylinder.

5.1.1. Summary of Findings

The findings for the influence of transfer port geometry on each output parameter are as follows:

- Scavenging efficiency: Scavenging efficiency remained unchanged throughout the variation of transfer port geometry and exhaust piston lead angle. The most significant change in scavenging efficiency was due to changes in swirl angle with only a 0.61% change and a sensitivity coefficient of 0.01.

- Trapping efficiency: Trapping efficiency was not influenced by changes to transfer port geometry but exhibited a dependence on exhaust piston lead angle. The sensitivity coefficients for transfer port geometry were 0.05 or less, while exhaust piston lead angle produced a coefficient of 0.18.
- Normalized swirl circulation: Normalized swirl circulation was influenced most strongly by transfer port geometry changes and varied regarding exhaust piston lead angle. The sensitivity coefficients for transfer port geometry were 0.60 and 0.74, while exhaust piston lead angle produced a coefficient of 0.11. Therefore, transfer port geometry influenced normalized swirl circulation five times more than exhaust piston lead angle.
- Normalized tumble circulation: Normalized tumble circulation was most significantly influenced by transfer port geometry. The sensitivity coefficients for transfer port geometry were 6.53 and 2.04. In comparison, the coefficient for exhaust piston lead angle was 0.51. As a result, normalized tumble circulation is four times more sensitive to transfer port geometry than exhaust piston lead angle.
- Normalized turbulent kinetic energy: Normalized TKE was affected by all three input parameters. At exhaust port closing, changes in transfer port geometry generated sensitivity coefficients of 0.76 and 0.75. Changes in exhaust piston lead angle produced a coefficient of 0.29.

5.2. Conclusions

Numerical modeling of a two-stroke, opposed-piston engine is a feasible method of predicting the behavior of in-cylinder flow while the charge exchange process takes place and during the combustion event. With a user-defined function, combustion and diffusion equations can be supplemented to the Fluent solver to obtain more realistic results. Also, the development of the numerical model allows the investigation of many different test cases without altering or financing a physical experiment.

During the investigation of the test cases, normalized tumble circulation proved to have the most interesting trends. For example, as tilt angle increased, the normalized tumble circulation decreased. Also, the normalized tumble circulation reversed when implementing low swirl angles.

Both results were explained by unexpected but physically feasible flow characteristics in the cylinder.

Another unique aspect of the model was the use of a blower on the engine by setting the inlet pressure to 101325 Pa gauge pressure. The use of the blower proved to boost scavenge efficiencies for all test cases. The lowest scavenging efficiency experienced was 99.3%.

Finally, this research project should be viewed as an initial model to test the theory of creating a 3D hot flow analysis for a two-stroke, opposed-piston engine. Additional improvements could be made to the model by improving the combustion behavior or adding additional species to the diffusion equations. Using this initial model, the research questions for this thesis research project were also answered.

5.3. Answer to Research Questions

Altering the transfer port geometry did not have a significant effect on scavenging efficiency or trapping efficiency. As discussed in Section 5.1.1, the sensitivity coefficient for transfer port geometry remained under 0.05 for engine efficiencies. Exhaust piston lead angle did not significantly affect scavenging efficiency but did alter the trapping efficiency of the engine. The sensitivity coefficient of trapping efficiency, due to changes in lead angle, was 0.18.

Altering the transfer port geometry and the exhaust piston lead angle produced significant changes in turbulence in the cylinder. Sensitivity coefficients from **Error! Reference source not found.** remained above 0.11 for all input parameter sweeps. The input parameters with the most influence on each output parameter were as follows: tilt and swirl angles influenced the turbulence parameters exclusively, while exhaust piston lead angle primarily affected trapping efficiency and normalized tumble circulation.

5.4. Recommendations

The numerical model developed for the thesis study proved to be effective at modeling the behavior of a two-stroke, opposed-piston engine. Each test case produced physically plausible results, and all unexpected trends in the data were explained by unexpected flow phenomena in the cylinder. Improvements could be made to the model to enhance accuracy by adding more advanced chemical kinetics for the combustion reaction. Also, the mesh domain could be expanded to include the entire cylinder as well as an intake plenum and exhaust system. Finally, the diffusion model could be updated to include more than two species for exhaust-fresh charge mixing.

After the sensitivity of each output parameter to each input parameter was determined, the optimal engine configuration was determined for the CFD model. Since engine efficiencies were only affected by exhaust piston lead angle, the optimal lead angle of 20 degrees was selected, as seen in Figure 4.27. This exhaust piston lead angle maximized the trapping efficiency of the engine.

Then, since normalized swirl circulation, normalized tumble circulation, and normalized turbulent kinetic energy were each sensitive to all three input parameters, the optimal tilt and swirl angle were selected from Figure 4.28, Figure 4.29, and Figure 4.30. Swirl angle was optimized at 15 degrees, where normalized TKE and normalized tumble circulation were maximized. This swirl angle did not maximize normalized swirl circulation, but normalized TKE and normalized tumble circulation fell after 15 degrees. The optimal tilt angle was selected using the most sensitive output, normalized tumble circulation. The optimal tilt angle occurred at 10 degrees.

Therefore, as determined by this study, the optimal engine configuration was 15 degrees swirl angle, 10 degrees tilt angle, and 20 degrees exhaust piston lead angle.

5.4.1. Future Work

Given more computational and model development time, the numerical model should be made more physically accurate. The following items are tasks that would alleviate weaknesses of the numerical model:

- Creating a physical test apparatus to validate the operation of the numerical model. This test would increase the validity of the numerical results and allow fine-tuning of the user-defined function.
- Expanding the numerical model's domain to include the entire cylinder-port configuration along with an intake and exhaust system. An intake system would especially benefit the model as it would allow more volume to absorb the pressure spikes when the ports open and close. Also, this would eliminate the periodic boundary condition used in the axisymmetric model.
- Modifying the user-defined diffusion model to include more than two species for mass diffusion. The addition of other combustion products would increase the accuracy of the mixing action with fresh air when the ports are open.

- Expanding the analysis to cover the entire input space of the model. This expansion would require 100 test cases to be run but would more accurately describe the influence of the input parameters.

REFERENCES

Achates Power and Cummins develop leap-ahead capability for the US Army Ground Combat Fleet. (2018, October 01). Retrieved September 15, 2020, from https://achatespower.com/achates-power-and-cummins-develop-leap-ahead-capability-for-the-us-army-ground-combat-fleet/

Achates showcases 2.7L, 3-cylinder opposed piston gasoline compression ignition engine in F-150; estimated 37 mpg combined. (2018, January 18). Retrieved November 23, 2020, from https://www.greencarcongress.com/2018/01/20180118-achates.html

Betz, D. (2001). *Physical mechanisms of *mixing* [Doctoral dissertation, University of California, Santa Barbara] (pp. 1-147). Ann Arbor, MI: Proquest Dissertations Publishing. Retrieved October 15, 2020, from https://www-proquest-com.ezproxy.lib.purdue.edu/docview/275752997?accountid=13360

Bird, R. B., Stewart, W. E., & Lightfoot, E. N. (2007). *Transport phenomena* (2nd edition). New York, NY: J. Wiley

Changlu, Z., Fujun, Z., Zhenfeng, Z., & Shuanlu, Z. (2015). Effects of Scavenging System Configuration on In-Cylinder Air Flow Organization of an Opposed-Piston Two-Stroke Engine. *Energies (Basel), 8*(6), 5866-5884. http://doi.org/10.3390/en8065866

Chen, N. H. & Othmer, D. F. (1962). New generalized equation for gas diffusion coefficient. *Journal of chemical and engineering data*, *7*(1), 37-41. http://doi.org/10.1021/je60012a011

Czyż, Z., Siadkowska, K., & Sochaczewski, R. (2019). CFD analysis of charge exchange in an aircraft opposed-piston diesel engine (p. 1-6). In J. Author (Comp.), *III International Conference of Computational Methods in Engineering Science*; Kazimierz Dolny, Poland, November 22-24, 2018. MATEC Web of Conferences. http://doi.org/10.1051/matecconf/201925204002

Dalla Nora, M., Lanzanova, T. D., & Zhao, H. (2018). Investigation of performance and combustion characteristics of a four-valve supercharged two-stroke DI engine fueled with gasoline and ethanol. *Fuel (Guildford)*, *227*(2), 401-411. http://doi.org/10.1016/j.fuel.2018.04.078

Department of Energy. (2020). *FY20 advanced vehicle technologies research funding oppportunity announcement.* Retrieved October 2020 from https://eere-exchange.energy.gov/FileContent.aspx?FileID=921c7f7c-482e-4390-872b-d739226a3d72

Environmental Protection Agency. (2020, September 9). *Sources of greenhouse gas emissions*. Greenhouse gas emissions. https://www.epa.gov/ghgemissions/sources-greenhouse-gasemissions.

Fontaras, G., Zacharof, N., & Ciuffo, B. (2017). Fuel consumption and CO2 emissions from passenger cars in Europe – Laboratory versus real-world emissions. *Progress in Energy and Combustion Science, 60*(4), 97-131. http://doi.org/10.1016/j.pecs.2016.12.004

Hooper, P., Al-Shemmeri, T., & Goodwin, M. (2011). Advanced modern low-emission two-stroke cycle engines. *Journal of Automobile Engineering, 225*(11), 1531-1543. http://doi.org/10.1177/0954407011408649

Huo, M., Huang, Y., & Hofbauer, P. (2015). Piston design impact on the scavenging and combustion in an opposed-piston, opposed-cylinder (OPOC) two-stroke engine (n.p.). In Dempsey, A. B., Johansson, B., Splitter, D. (Comp.), *SAE Technical Paper: Proceedings of the SAE 2015 World Congress & Exhibition*; Detroit, MI, April 21-23, 2015. SAE International. http://doi.org/10.4271/2015-01-1269

Kirkpatrick, A. (1999). *Simple finite heat release model*. Thermodynamics. https://www.engr.colostate.edu/~allan/thermo/page6/page6.html

Kozal, L. (2017). *Design of an opposed-piston, opposed-stroke diesel engine for use in utility aircraft* [Unpublished master's thesis]. University of Dayton. Retrieved October 17, 2020, from https://ecommons.udayton.edu/cgi/viewcontent.cgi?article=1108&context=uhp_theses

Kundu, P. K., Cohen, I. M., & Hu, H. H. (2004). *Fluid mechanics* (3rd edition). Amsterdam; Elsevier Academic Press.

Liu, J., & Dumitrescu, C. E. (2019). Single and double wiebe function combustion model for a heavy-duty diesel engine retrofitted to natural-gas spark-ignition. *Applied Energy, 248*(1), 95-103. https://doi.org/10.1016/j.apenergy.2019.04.098

Mattarelli, E., Rinaldini, C., Savioli, T., Cantore, G., Warey, A., Potter, M., Gopalakrishnan, V., & Balestrino, S. (2017). Scavenge ports optimization of a 2-stroke opposed piston diesel engine (n.p.). In J. Author (Comp.), *SAE Technical Papers: Proceedings of the 13th International Conference on Engines and Vehicles*; Capri, Italy, September 10-14, 2017. SAE International. http://doi.org/10.4271/2017-24-0167

Morton, R., Riviere, R., & Geyer, S. (2017). Understanding limits to the mechanical efficiency of opposed piston engines (n.p.). In J. Author (Comp.), *SAE Technical Papers: Proceedings of the SAE World Congress Experience*; Detroit, MI, April 4-6, 2017. SAE International. http://doi.org/10.4271/2017-01-1026

NASA. (2015). *The cost of energy, environmental impact*. What you need to know about energy. http://needtoknow.nas.edu/energy/energy-costs/environmental/.

National Academy of Sciences. (2014). *Climate Change: Evidence and Causes*. The National Academies Press. https://doi.org/doi:10.17226/18730

Pirault, J. P., & Flint, M. (2010). *Opposed piston engines: evolution, use, and future applications*. Warrendale, PA: Society of Automotive Engineers

Růžička, P. (2018). Modeling of boundary layer and the influence on heat transfer with help of CFD. *American Institute of Physics*, *2047*(1), 1-12. http://doi.org/10.1063/1.5081654

Saltelli, A., Aleksankina, K., Becker, W., Fennell, P., Ferretti, F., Holst, N., Li, S., & Wu, Q. (2019). Why so many published sensitivity analyses are false: A systematic review of sensitivity analysis practices. *Environmental Modelling & Software, 114*(2), 29-39. https://doi.org/10.1016/j.envsoft.2019.01.012

Saltelli, A., Ratto, M., Andres, T., Campolongo, F., Cariboni, J., Gatelli, D., Saisana, M., & Tarantola, S. (2008). *Global sensitivity analysis. The primer*. Chichester, England: John Wiley & Sons.

Stern, F., Wilson, R. V., Coleman, H. W., & Paterson, E. G. (2001). Comprehensive approach to verification and validation of CFD simulations - Part 1: Methodology and procedures. *Journal of Fluids Engineering, 123*(4), 793–802. http://doi.org/10.1115/1.1412235

Thomas, G. (2009). *CFD modelling and analysis of an opposed piston internal combustion engine* [Unpublished master's thesis]. University of Wollongong. Retrieved October 19, 2020, from https://ro.uow.edu.au/cgi/viewcontent.cgi?article=4098&context=theses

Turns, S. R. (2012). *An introduction to combustion: Concepts and applications* (3rd edition). New York, NY: McGraw-Hill.

U.S. Energy Information Administration. (2019). *International energy outlook 2019*. Retrieved November 2020 from https://www.eia.gov/todayinenergy/detail.php?id=41433

United Nations – Population Division. (2019). *Historic and projected population*. Retrieved November 2020 from https://ourworldindata.org/grapher/historic-and-projected-population?tab=chart&stackMode=absolute&time=earliest..latest&country=OWID_WRL-0~OWID_WRL-1&region=World

Xu, S., Wang, Y., Zhu, T., Xu, T., & Tao, C. (2011). Numerical analysis of two-stroke free piston engine operating on HCCI combustion. *Applied Energy, 88*(11), 3712-3725. http://doi.org/10.1016/j.apenergy.2011.05.002

Zhenfeng, Z., Yangang, Z., Jun, W., Yaonan, F., Tiexiong, S., Yi, Z., & Yuhang, L. (2017). Simulation modeling method and experimental investigation on the uniflow scavenging system of an opposed-piston folded-cranktrain diesel engine. *Energies (Basel), 10*(5), 727. http://doi.org/10.3390/en10050727

Zielinski, J., Andreucci, R., Rajagopalan, N., & Aktas, C. B. (2018). Prospects for meeting the corporate average fuel economy standards in the U.S. resources. *Conservation and Recycling*, *136*(3), 466-472. http://doi.org/10.1016/j.resconrec.2018.03.026

APPENDIX A. USER-DEFINED FUNCTION CODE

```
/*********************************************************************
UDF for calculating heat release in dynamic mesh IC engine simulation.

C-code below written by Beau Burbrink/Jason Ostanek on January 26, 2021

*********************************************************************/

#include "udf.h"              /* needed for UDF macros (e.g. DEFINE) */
#include "unsteady.h"         /* needed for time-dependent macros (e.g.
CURRENT_TIME) */
#include "prf.h"              /* needed for global macros (e.g. PRF_GRSUM1)
*/
#include "dynamesh_tools.h"   /* needed for dynamic mesh tools (e.g.
TIME_TO_ABSOLUTE_CRANK_ANGLE) */

/* Problem setup parameters */
#define threadID_cc 10        /* Combustion Chamber Zone ID */
#define threadID_ip 13        /* Intake Piston Zone ID */
#define threadID_ep 14        /* Exhaust Piston Zone ID */
int threadID_ar[] = {threadID_cc, threadID_ip, threadID_ep};

real rpm, CA_step, CA;                                 /* in cylinder
initialization */
real CA_burned = 162, delta_CA = 30, CA_0 = 160;       /* crank angle
parameters */
real LHV_fuel = 43400000, eta_comb = 0.9, AFR = 14.7; /* fueling parameters
*/
real a = 5, m = 2;                                     /* Wiebe parameters */
real m_fuel, m_air, m_air_unburned;                    /* Initialize cylinder
mass variables */
real vol, vol_M1;                                      /* Cylinder volume
variables */
real Q, dQ, dQCA;                                      /* Heat release
variables */
real Wb, dWb, dBF;                                     /* Wiebe function
variables */

DEFINE_EXECUTE_ON_LOADING(memname, libname)
{
  Set_User_Memory_Name(0,"Q (J)");                     /* Set up user-defined
memory for ANSYS Fluent... */
  Set_User_Memory_Name(1,"dQ (W/m^3/s)");              /* to allow access to
UDF values from Fluent */
  Set_User_Memory_Name(2,"CA (deg)");
  Set_User_Memory_Name(3,"dQCA (J/deg)");
  Set_User_Memory_Name(4,"D_AB (m^2/s)");
  Set_User_Memory_Name(5,"Mass (kg)");
  Set_User_Memory_Name(6,"Unburned Mass (kg)");
}

DEFINE_SOURCE(src_Q,c,t,dS,eqn)
{
```

```
	real heat;		/* This function returns the heat transfer
rate... */
				/* from the Wiebe model calculations as a heat
source */
	heat = C_UDMI(c,t,1);

	dS[eqn] = 0;		/* Handle source term explicitly */

	return heat;
}

DEFINE_INIT(init_vol,d)
{
	/* Initialize variables */
	int i;
	vol = 0;
	m_air = 0;
	m_air_unburned = 0;

	#if !RP_HOST

		/* Calculate chamber values through sum of each cell */
		for (i = 0; i < 3; i++) {
			Thread *t = Lookup_Thread(d, threadID_ar[i]);
			cell_t c;
			begin_c_loop_int(c, t)
			{
				vol += C_VOLUME(c, t);		/* Calculate
cylinder volume */
				m_air += C_R(c, t) * C_VOLUME(c, t); /* Calculate
mass of charge in cylinder */

				/* Calculate mass of unburned air in cylinder */
				m_air_unburned += C_R(c, t) * C_VOLUME(c, t) *
			C_YI(c, t, 1);
			}
			end_c_loop_int(c, t)
		}

	#if RP_NODE
		vol = PRF_GRSUM1(vol);
		m_air = PRF_GRSUM1(m_air);
		m_air_unburned = PRF_GRSUM1(m_air_unburned);
	#endif

	#endif

	node_to_host_real_3(vol, m_air,m_air_unburned);

	/* Update User-Defined Memory */
	for (i = 0; i < 3; i++) {
		Thread* t = Lookup_Thread(d, threadID_ar[i]);
		cell_t c;
		begin_c_loop_int(c, t)
		{
			C_UDMI(c, t, 5) = m_air;
			C_UDMI(c, t, 6) = m_air_unburned;
```

```
		}
		end_c_loop_int(c, t)
	}
}

DEFINE_ADJUST(adjust,d)
{
	/* Adjust function for chamber */
	real time = DYNAMESH_CURRENT_TIME, CA_act, m_air_corrected, m_air_save;
	int i;

	/* Initialize variables */
	vol = 0;
	m_air = 0;
	m_air_unburned = 0;
	rpm = RP_Get_Real("dynamesh/in-cyn/crank-rpm");	/* engine speed
*/
	CA_step = RP_Get_Real("dynamesh/in-cyn/delta-angle"); /* crank angle
step */

	/* Correct crank angle for to be periodic from 0-360 for all three
cycles */
	CA_act = TIME_TO_ABSOLUTE_CRANK_ANGLE(time);
	if (CA_act < (360 + CA_step / 2)) {
		CA = CA_act;
	}
	else if (CA_act > (360 - CA_step / 2) && CA_act < (720 - CA_step / 2))
{
		CA = CA_act - 360;
	}
	else if (CA_act > (720 - CA_step / 2)) {
		CA = CA_act - 720;
	}

	#if !RP_HOST

		/* Calculate chamber values */
		for (i = 0; i < 3; i++) {
			Thread *t = Lookup_Thread(d, threadID_ar[i]);
			cell_t c;
			begin_c_loop_int(c, t)
			{
				vol += C_VOLUME(c, t);		/* Calculate
cylinder volume */
				m_air += C_R(c, t) * C_VOLUME(c, t); /* Calculate
mass of charge in cylinder */

				/* Calculate mass of unburned air in cylinder */
				m_air_unburned += C_R(c, t) * C_VOLUME(c, t) *
			C_YI(c, t, 1);
			}
			end_c_loop_int(c, t)
		}

	#if RP_NODE
		vol = PRF_GRSUM1(vol);
```

```
            m_air = PRF_GRSUM1(m_air);
            m_air_unburned = PRF_GRSUM1(m_air_unburned);
      #endif

      #endif

      node_to_host_real_3(vol, m_air, m_air_unburned);

      /* Calculate Heat Source Term [W/m^3]*/

      /* Wiebe Function */
      if((CA >= (CA_0 - 2) && CA <= (CA_0 - 1))) {
            m_air_save = m_air_unburned;
      }
      if((CA >= CA_0 && CA <= (CA_0 + delta_CA))) {
            Wb = 1-exp(-a * pow(((CA-CA_0) / delta_CA),(m+1)));         /*
Calculate wiebe model value */

            /* Calculate wiebe model derivative */
            dWb = ((1- Wb)*(m+1)*a)/delta_CA * pow(((CA-CA_0)/delta_CA),m);

            m_air_corrected = m_air_save;                               /*
      Retain full mass for fuel calc */

      }
      else{
            Wb = 0;
            dWb = 0;
            m_air_corrected = m_air_unburned;
      }

      /* Heat Term */
      m_fuel = m_air_corrected / (AFR+1);       /* Calculate fuel mass using
unburned mass and AFR */
      dBF = dWb*m_air_corrected*6*rpm/vol;            /* Calculate transfer
rate of species during burning */

      dQ = dWb*m_fuel*LHV_fuel*eta_comb*6*rpm/vol;    /* Calculate heat
transfer rate [W/m^3] */
      dQCA = dWb*m_fuel*LHV_fuel*eta_comb;            /* Calculate heat
transfer rate [J/m^3/deg] */

      Q = Wb*m_fuel*LHV_fuel*eta_comb;          /* Calculate heat transfer
[J] */

      /* Update User-Defined Memory */
      for (i = 0; i < 3; i++) {
            Thread *t = Lookup_Thread(d, threadID_ar[i]);
            cell_t c;
            begin_c_loop_int(c, t)
            {
                  C_UDMI(c, t, 0) = Q;
                  C_UDMI(c, t, 1) = dQ;
                  C_UDMI(c, t, 2) = CA;
                  C_UDMI(c, t, 3) = dQCA;
                  C_UDMI(c, t, 5) = m_air;
                  C_UDMI(c, t, 6) = m_air_unburned;
```

```
            }
            end_c_loop_int(c, t)
        }

}

DEFINE_DIFFUSIVITY(diffusion_coeff,c,t,i)
{
        /* Function to calculate mass diffusivity coefficient,
        needs to calculate for only a single cell (no loop required) */

        /* Define variables and cell properties (A=Air, B=CO2) */
        real D_AB;
        real T = C_T(c,t), P = C_P(c,t) + RP_Get_Real("operating-pressure");

        /* Lennard-Jones Parameters*/
        real M_A = 28.97, M_B = 44.01;                  /* molar mass */
        real sigma_A = 3.55, sigma_B = 4.49;            /* lennard-jones */
        real epsilon_A = 106, epsilon_B = 189;          /* lennard-jones */

        /* Experimental fit for collision integral */
        real A=1.06036, B=0.15610, C=0.19300, D=0.47635, E=1.03587, F=1.52996,
G=1.76474, H=3.89411;

        real sigma_AB, epsilon_AB, T_star, omega_AB;    /* initialize combined
lennard-jones */

        sigma_AB = 0.5*(sigma_A + sigma_B);       /* lennard-jones combination
law */
        epsilon_AB = sqrt(epsilon_A*epsilon_B);   /* lennard-jones combination
law */

        /* Calculate collision integral */
        T_star = T/epsilon_AB;
        omega_AB = A/pow(T_star,B) + C/exp(D*T_star) + E/exp(F*T_star) +
G/exp(H*T_star);

        /* Calculate diffusion coefficient (mass diffusivity) */
        D_AB = 188.29*pow(10,-
4)*sqrt(pow(T,3)*(1/M_A+1/M_B))*1/(P*pow(sigma_AB,2)*omega_AB);

        C_UDMI(c,t,4) = D_AB;                     /* store coefficient in user-
defined memory */

        return D_AB;
}

DEFINE_EXECUTE_AT_END(patch_UDS)
{
        /* Function to patch cells to burned gas when combustion is complete */
        int i;
        Domain *d;
        d = Get_Domain(1);

        /* Adjust UDS at Specified Crank Angle */
```

```
	if (CA > (CA_0 + delta_CA - CA_step / 2) && CA < (CA_0 + delta_CA + 
CA_step / 2)) {

		/* Change scalar of cells */
		for (i = 0; i < 3; i++) {
			Thread *t = Lookup_Thread(d, threadID_ar[i]);
			cell_t c;
			begin_c_loop_int(c, t)
			{
				C_YI(c, t, 0) = 1;
			}
			end_c_loop_int(c, t)
		}
	}
}

DEFINE_SPECIFIC_HEAT(air_Cp, T, Tref, h, yi)
{
	real Cp, A0, A1, A2, A3, A4, A5, A6, A7;

	A7 = 0.;
	A6 = 0.;
	A5 = -1.142077E-13;
	A4 = 7.658085E-10;
	A3 = -1.924449E-06;
	A2 = 2.174350E-03;
	A1 = -8.816731E-01;
	A0 = 1.121599E+03;

	Cp = A7 * pow(T, 7) + A6 * pow(T, 6) + A5 * pow(T, 5) + A4 * pow(T, 4) 
+ A3 * pow(T, 3) + A2 * pow(T, 2) + A1 * pow(T, 1) + A0;

	*h = Cp * (T - Tref);

	return Cp;
}

DEFINE_PROPERTY(air_mu, c, t)
{
	real mu, T, A0, A1, A2, A3, A4, A5, A6, A7;

	A7 = 0.;
	A6 = 0.;
	A5 = 2.174496E-21;
	A4 = -1.519981E-17;
	A3 = 4.221365E-14;
	A2 = -6.353860E-11;
	A1 = 7.558631E-08;
	A0 = 5.240530E-07;

	T = C_T(c, t);

	mu = A7 * pow(T, 7) + A6 * pow(T, 6) + A5 * pow(T, 5) + A4 * pow(T, 4) 
+ A3 * pow(T, 3) + A2 * pow(T, 2) + A1 * pow(T, 1) + A0;

	return mu;
}
```

```
DEFINE_PROPERTY(air_k, c, t)
{
	real k, T, A0, A1, A2, A3, A4, A5, A6, A7;

	A7 = 0;
	A6 = 0;
	A5 = 7.431298E-21;
	A4 = -4.922373E-17;
	A3 = 4.760862E-12;
	A2 = -2.915444E-08;
	A1 = 9.050351E-05;
	A0 = 9.920017E-04;

	T = C_T(c, t);

	k = A7 * pow(T, 7) + A6 * pow(T, 6) + A5 * pow(T, 5) + A4 * pow(T, 4) +
A3 * pow(T, 3) + A2 * pow(T, 2) + A1 * pow(T, 1) + A0;

	return k;
}
```